

Mechanical Intelligence Simplifies Control in Terrestrial Limbless Locomotion

Tianyu Wang,^{1,2,†} Christopher Pierce,^{1,3,†} Velin Kojouharov,⁴ Baxi Chong,¹
Kelimar Diaz,¹ Hang Lu,² Daniel I. Goldman^{1,*}

¹School of Physics, Georgia Institute of Technology,
837 State St NW, Atlanta, GA 30332, USA

²Institute for Robotics and Intelligent Machines, Georgia Institute of Technology,
801 Atlantic Dr NW, Atlanta, GA 30332, USA

³School of Chemical & Biomolecular Engineering, Georgia Institute of Technology,
311 Ferst Dr, Atlanta, GA 30332, USA

⁴George W. Woodruff School of Mechanical Engineering, Georgia Institute of Technology,
801 Ferst Dr NW, Atlanta, GA 30318, USA

*To whom correspondence should be addressed; E-mail: daniel.goldman@physics.gatech.edu.

†These authors contributed equally to this work.

Abstract:

Limbless locomotors, from microscopic worms to macroscopic snakes, traverse complex, heterogeneous natural environments typically using undulatory body wave propagation. Theoretical and robophysical models typically emphasize body kinematics and active neural/electronic control. However, we contend that because such approaches often neglect the role of passive, mechanically controlled processes (i.e., those involving *mechanical intelligence*), they fail to reproduce the performance of even the simplest organisms. To discover principles of how mechanical intelligence aids limbless locomotion in heterogeneous terradynamic regimes, here we conduct a comparative study of locomotion in a model of heterogeneous terrain (lattices of rigid

posts). We use a model biological system, the highly studied nematode worm *C. elegans*, and a novel robophysical device whose bilateral actuator morphology models that of limbless organisms across scales. The robot's kinematics quantitatively reproduce the performance of the nematodes with purely open-loop control; mechanical intelligence simplifies control of obstacle navigation and exploitation by reducing the need for active sensing and feedback. An active behavior observed in *C. elegans*, undulatory wave reversal upon head collisions, robustifies locomotion via exploitation of the systems' mechanical intelligence. Our study provides insights into how neurally simple limbless organisms like nematodes can leverage mechanical intelligence via appropriately tuned bilateral actuation to locomote in complex environments. These principles likely apply to neurally more sophisticated organisms and also provide a new design and control paradigm for limbless robots for applications like search and rescue and planetary exploration.

Summary:

A comparative biological and robotic study reveals principles of mechanical intelligence in terrestrial limbless locomotion.

Main text:

INTRODUCTION

Organisms from flapping hawkmoths (1) to prancing gazelles (2) to undulating snakes (3) and nematodes (4) produce directed movement through a combination of neural and mechanical control. Neural circuits integrate and process sensory information to produce locomotor commands through complex signaling networks. This helps organisms produce directed movement despite the constantly changing external environment by modulating motor com-

mands in response to environmental cues. Much progress has been made in understanding the neural aspects of locomotor control including the structure, function, and dynamics of neural circuits, particularly with genetic models such as *Caenorhabditis elegans* (5), *Drosophila melanogaster* (6), zebrafish (7) and mice (8).

In addition to purely neural control, “neuromechanical” approaches have been developed to describe the interaction between active neuronal controls and purely mechanical processes arising from body-environment interactions. This approach has been applied primarily to flying and walking systems (1, 9, 10). For example, fruit flies have been found to recover from flight disturbances through reflexive turning responses to mechanical stimuli (11), while running guineafowl have been shown to stabilize their gaits in rough terrain through passive adaptive responses (“preflexes”) mediated by the non-linear properties of the musculature (12). In general, body-environment interactions can help coordinate the movements of the body itself, through purely mechanical control processes, a phenomenon known as *mechanical* or *physical* intelligence (13). A complete description of organismal locomotion must therefore place principles of neural/computational intelligence and mechanical intelligence on an equal footing, leading to the concept of embodied intelligence (14–16).

While much attention has been paid to mechanical intelligence in legged and aerial systems, less is known about the interplay of neural and mechanical control in limbless locomotion. This locomotor strategy occurs within diverse and often highly complex, heterogeneous environments and spans length scales, from meter-long snakes (17, 18) with over 10^6 neurons to the millimeter-long nematode *Caenorhabditis elegans* (Fig. 1A), which navigates complex micro-environments like rotting fruit (Fig. 1C, Movie S1) with only 302 neurons (19, 20). Across the taxonomic and neuroanatomical diversity of lateral undulators, many organisms employ similar actuation mechanisms, including snakes and nematodes – bilaterally arranged bands of muscle which propagate waves of contralateral activation down the body. The ubiquity and biological

diversity of undulation, the continual environment-body hydro and terradynamic interactions, and the presence of common mechanisms of actuation suggest an important role for mechanical intelligence in limbless locomotion.

Given the importance of mechanics and the challenges of modeling locomotor interactions, using robots as “robophysical” models to identify key neuromechanical principles is appealing (21–23). These models incorporate simplified descriptions of organismal mechanics and neural control, and thus can be used to elucidate the emergent “template-level” dynamics of organisms (24). This approach has been particularly successful in identifying the role of mechanical control in legged locomotion, including hopping (25), bipedal (26), quadrupedal (27) and hexapodal (28) locomotion; and later flapping flight (29). These “terradynamic” systems have forced researchers to confront the remarkable unpredictability, non-linearity and heterogeneity of the physical world. However, these concepts have been less extensively applied in modelling the complex terradynamic interactions and biomechanics of limbless locomotion.

Limbless robots, despite often being referred to as snake-like (30–33), have yet to match the locomotion capabilities of even the simplest limbless organisms like nematodes. Existing limbless robots which often rely on complex and high bandwidth sensing and feedback (34–36) are stymied by unpredictable terrain in the real world that would not challenge their organismal counterparts (3, 19, 37). Beyond rigid systems, soft limbless robots with intrinsically compliant bodies have emerged over the last decade (38–40). However, control challenges that arise from air/fluid handling mechanisms and difficulties of modeling and modulating intrinsic material properties have limited their practical uses. Hence limbless robots have yet to fulfill their promised potential for agile movement in the type of complex environments encountered in applications such as search and rescue and planetary exploration. One feature of elongate vertebrate and invertebrates that is absent in the direct spinal actuation (joint actuation) design paradigm of limbless robots (32, 33) is bilateral actuation. Although simpler in design

and control, the joint actuation mechanism limits such devices in offering insights into possible functional roles of bilateral actuation. Indeed, recent work has implied the importance of bilateral actuation in snakes (3) and limbless devices (41–43) when interacting with heterogeneities, suggesting that such actuation can act as a mechanical intelligence and thereby simplifying control.

To advance our understanding and discover principles of mechanical intelligence in limbless locomotion, we took a comparative biological and robophysical approach, using two complementary models: a biological model, the nematode *Caenorhabditis elegans*, and a robophysical model, a limbless robot incorporating bilateral actuation that allows programmable and quantifiable dynamic body compliance and passive body-environment interactions. Therefore, mechanical intelligence can be isolated from active controls and be systematically tuned and tested. Comparisons between the kinematics and locomotor performance of our biological and robophysical models reveal that mechanical intelligence alone is sufficient for an open-loop limbless robot to reproduce the performance of nematodes. It simplifies controls in terrestrial limbless locomotion by taking advantage of passive body-environment interactions that enable heterogeneity negotiation, thereby stabilizing locomotion. Further, we showed that a simple *active* behavior inspired by nematodes takes advantage of mechanical intelligence to enhance locomotion performance even further. Our method and results not only provide insight into the functional mechanism of mechanical intelligence in organismal limbless locomotion but also provide a new paradigm for limbless robot development that simplifies control in complex environments.

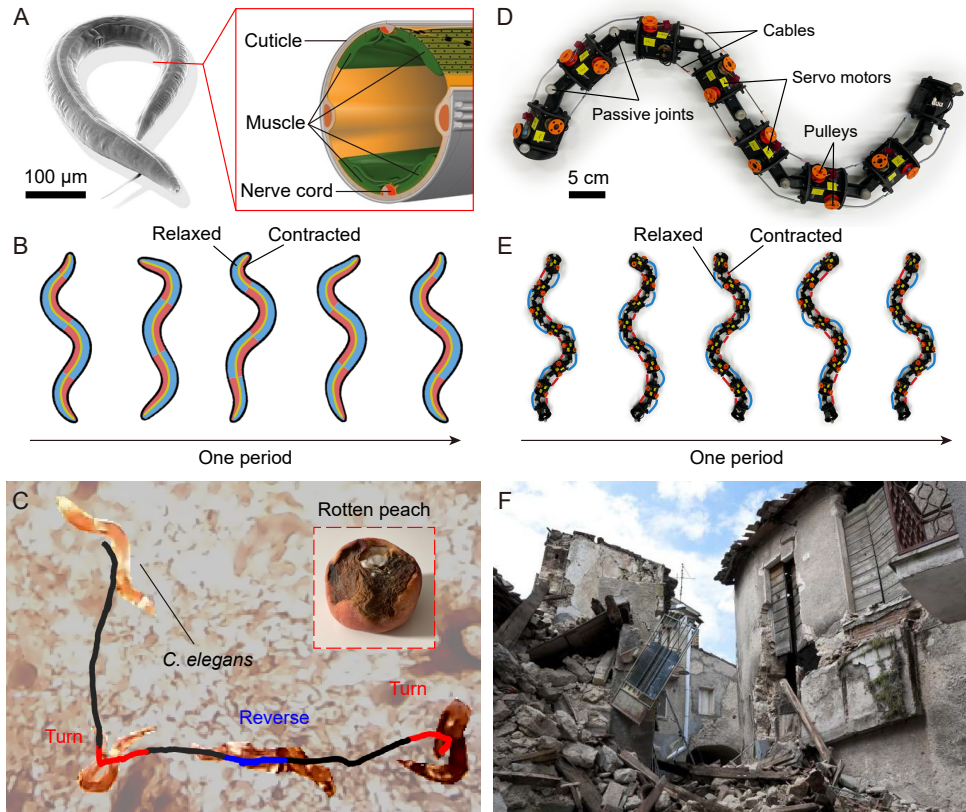


Fig. 1: Biological and robophysical systems for understanding mechanical intelligence in limbless locomotion. (A) Nematode *Caenorhabditis elegans*, the biological model of this study, along with a cross-section anatomy showing two pairs of bilaterally activated muscle bands. (B) Schematics of body postures and muscle activities over one gait period in the biological model. (C) A nematode moves on a slice of the rotten peach, a rheologically and mechanically complex natural environment. (D) The limbless robophysical model, implementing a bilaterally actuation mechanism. (E) Schematics of body postures and cable activities over one gait period in the robophysical model. (F) An example complex environment where limbless robotic devices have potentials to perform agile locomotion (credit: CC0 Public Domain).

RESULTS

Nematode kinematics and performance that implies mechanical intelligence

C. elegans (Fig. 1A) has a fully mapped nervous system (5, 44) with a variety of available genetic tools for perturbing (45) and observing (46) neuromuscular dynamics. Compared to

vertebrate undulators like snakes, its neural control architectures are simpler, and better understood. Moreover, the limited information we have about its ecology and environment suggests it is capable of contending with extremely varied and complex terrain like that in the interior of rotten fruit (19) (Fig. 1B). Hence it is a promising model for understanding how neural feedback control and mechanical intelligence interact to generate limbless locomotion. We studied *C. elegans* locomotion kinematics using microfluidic hexagonal pillar arrays (lattices) with varying pillar density as model heterogeneous environments (Fig. 2A-i, iv and vii, Movie S1). These arrays capture aspects of the confinement and hindrance to locomotion that natural heterogeneity can impose.

To simplify the analysis of locomotion kinematics in lattices, we exploit dimensionality reduction techniques. Prior work applied principal component analysis to study undulating systems, such as nematodes and snakes, and illustrated that the majority of body postures can be described by linear combinations of sine-like shape-basis functions, despite the inherently high dimensionality of postural data (47, 48). By considering the first two dominant shape basis functions (Fig. S2), we assume that the essence of the body-curvature profile κ at time t and location s ($s = 0$ denotes head and $s = 1$ denotes tail) can be approximated by:

$$\kappa(s, t) = w_1(t) \sin(2\pi\xi s) + w_2(t) \cos(2\pi\xi s), \quad (1)$$

where ξ is the spatial frequency of body undulation obtained from direct fitting. $w_1(t)$ and $w_2(t)$ are the reduced shape variables describing the instantaneous shape of the locomotor at time t . Thus, the locomotion may be visualized as a path through a two-dimensional “shape space” defined by w_1 and w_2 (details are provided in Materials and Methods).

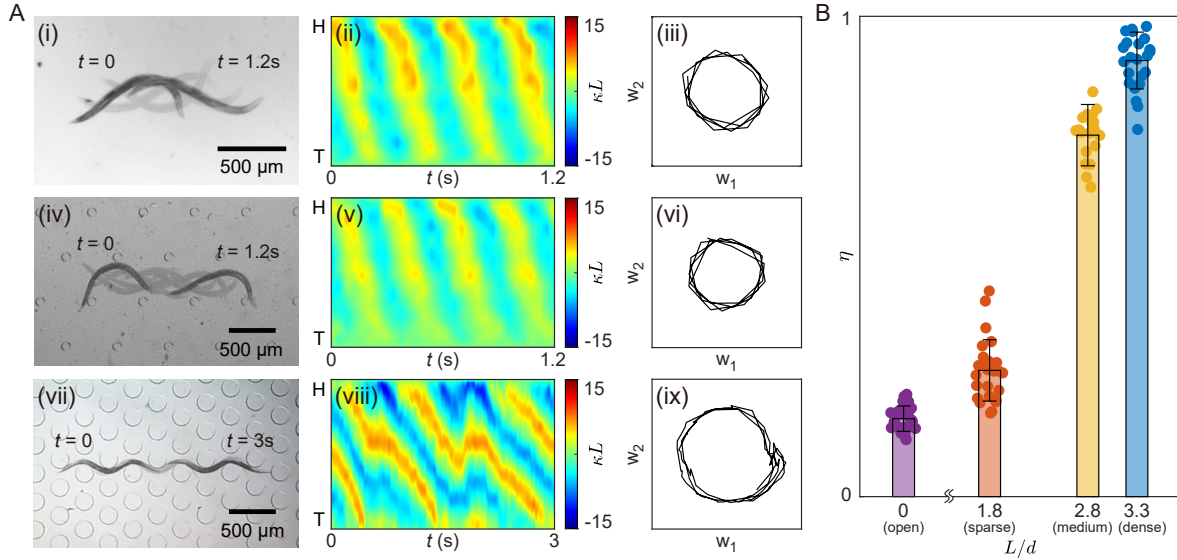


Fig. 2: Nematode kinematics and locomotor performance implies the role of mechanical intelligence in organismal limbless locomotion. **(A)** Overlaid snapshots, effective body curvature and gait paths in the shape space of nematode locomotion in laboratory environments with varied pillar density. **(B)** Locomotion speed (wave efficiency η) as a function of obstacle density (measured as the ratio of body length and obstacle spacing L/d) for nematodes

We assessed nematode locomotion in four environments with varying pillar density, $L/d = 0$ (open fluid), 1.8 (sparse lattice), 2.8 (medium lattice), and 3.3 (dense lattice), where L represents nematode body length and d denotes pillar spacing. As previously noted (49), nematodes perform an approximate traveling wave motion in homogeneous open fluid. In the shape space, this leads to circular orbits, where one full rotation corresponds to a single undulation cycle (Fig. 2A-i to iii). The nematode maintains a traveling-wave-like gait in all lattice spacings, despite pitch differences. In sparser lattices (Fig. 2A-iv to vi), the body kinematics are similar to those in a bulk fluid. Only in the dense lattice (Fig. 2A-vii to ix) do we observe deviations from an ideal travelling wave. However, these deviations are small and transient, so that the overall path in shape space remains mostly circular. These deformations are typically correlated with body deformations induced by collisions (typically between the head and an obstacle) and rapidly ($\sim 0.4s$) return to smooth traveling wave motion. Thus, environmental heterogeneities

can induce small perturbations that converge back to a stable circular orbit, suggesting that the basic strategy of propagating traveling waves along the body is robust to intrusions by obstacles.

We further systematically evaluated nematode locomotor performance in terms of locomotion speed, measured by the wave efficiency η , the ratio of forward center of mass speed to the wave propagation speed (Fig. 2B). We noticed that thrust-producing interactions with pillars produce larger η relative to the free swimming case (50), despite the similarity of the kinematics. As pillar density increases, by contrast, wave periodicity is frequently disrupted by inhibitory interactions (i.e., producing force opposite the direction of travel), typically coinciding with interactions between the nematode's head and a pillar. However, in the densest lattices, bouts of smooth traveling wave propagation between head interactions display an overall increase in η . In this regime the nematode can take advantage of thrust-producing interactions with the lattice to increase η but avoids inhibitory collisions that would lead to jamming and getting stuck. We hypothesize that the mechanism of stabilization is primarily passive in nature, and mechanical intelligence is sufficient for heterogeneity negotiation, without the need of explicit modulations of body postures.

Robophysical model development for investigating mechanical intelligence

To test if mechanical intelligence alone is sufficient to reproduce the performance of nematode lattice traversal, we developed a hard-soft hybrid robophysical model (86 cm long with 7 bending joints) which models the bilateral actuation scheme of nematodes and other limbless organisms, actuating joints by contracting and relaxing cables via decentralized cable-pulley-motor systems (each cable is independently controlled) on either side of each joint (Fig. 1D, Movie S2). By properly coordinating the lengths of cables through waves of angular oscillation passing along the body, the robophysical model can produce similar undulatory locomotion as limbless organisms (Fig. 1B, E). Although its movements are slower than those of limbless

organisms, the highly damped nature of the locomotion in both systems (viscous in the nematodes, frictional in the robot) allows the robophysical model to offer insight into the function of mechanical intelligence in complex terrain navigation in the organism.

The bilateral cable actuation mechanism enables body compliance in the robophysical model. However, differing from soft limbless robots that inherit compliance from soft materials which is usually hard to modulate, cables in our robophysical model are non-elastic, and thus their lengths can be explicitly controlled. This allows the body compliance in our robophysical model to be quantifiable, programmable, inhomogeneous and anisotropic, simply by coordinating the lengthening and shortening of cables. To implement a basic traveling-wave locomotion pattern on the robophysical model as observed in nematodes, we developed the control scheme based on the “serpenoid” shape-based template (51). The template generates a central pattern that enables a wave to propagate from head to tail, if the i -th joint angle α_i in the spine at time t follows

$$\alpha_i(t) = A \sin(2\pi\xi \frac{i}{N} - 2\pi\omega t), \quad (2)$$

where A , ξ and ω is the amplitude, the spatial and temporal frequencies of the wave, i is the joint index, and N is the total number of joints. The joint angle α given by this template will be further referred to as the “suggested” angle.

To describe the degree of body compliance, we introduce a variable, generalized compliance $G \in [0, +\infty)$. When $G = 0$, we contract all cables so that joints are non-compliant, resisting forces from either sides. Thus joint angles can precisely track the suggested angles. The projection of joint angle trajectories in the configuration space to the shape space (following the method given by Eq. 1) then is a perfect circular orbit (Fig. 3A). Specifically, at $G = 0$ the robophysical model behaves as a conventional rigid limbless robots. We note the exact lengths of the left and right cables that form an angle α_i on the i -th joint as $\mathcal{L}_i^l(\alpha_i)$ and $\mathcal{L}_i^r(\alpha_i)$ (see Material and Method for full derivation of \mathcal{L}_i^l and \mathcal{L}_i^r based on robophysical model geometry).

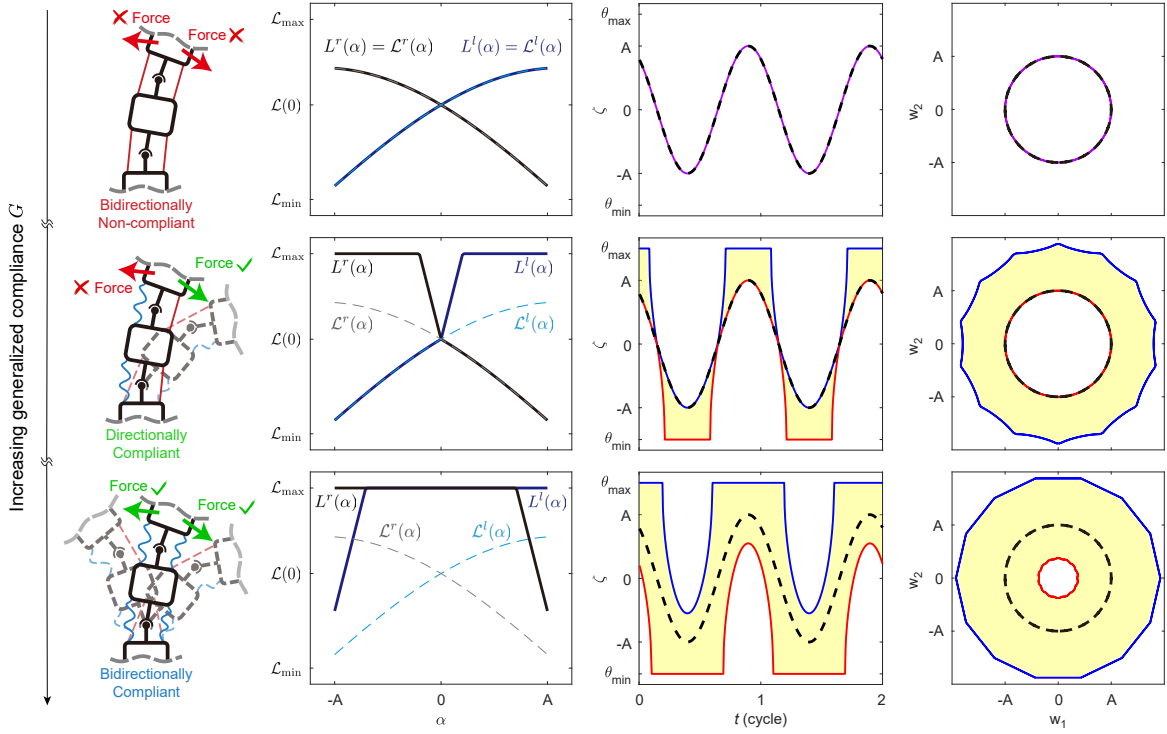


Fig. 3: Programmable and quantifiable body compliance in the bilaterally actuated robophysical model for investigating the functional mechanism of mechanical intelligence. Three representative compliant states of the robophysical model under varied generalized compliance G : bidirectionally non-compliant (A), directionally compliant (B) and bidirectionally compliant (C). The first column illustrates schematics of cable activation, where red cables are contracted while blue cables are relaxed. The second column shows how cables are relaxed at varied suggested angles according to the control scheme, where solid lines represent implemented cable lengths while dashed lines represent “exact” lengths of cables to form the suggested angle. The third column shows how much a feasible emergent angle ζ (yellow region) is allowed to deviate from the suggested angle α (dashed line), where solid blue and red lines represent upper and lower boundaries of ζ . The last column shows the how much a feasible emergent gait path in the shape space (yellow region) is allowed to deviate from the suggested circular gait path (dashed line), where solid blue and red lines represent outer and inner boundaries of feasible emergent gait paths.

When G is non-zero, we control the lengths of the left and right cables $L_i^{l/r}$ for the i -th joint

following

$$\begin{aligned}
L_i^l(\alpha_i) &= \begin{cases} \mathcal{L}_i^l(\alpha_i) & \text{if } \alpha_i \leq -(2G_i - 1)A \\ \mathcal{L}_i^l[-A \cdot \min(1, 2G_i - 1)] + l_0 \cdot [(2G_i - 1)A + \alpha_i] & \text{if } \alpha_i > -(2G_i - 1)A \end{cases} \\
L_i^r(\alpha_i) &= \begin{cases} \mathcal{L}_i^r(\alpha_i) & \text{if } \alpha_i \geq (2G_i - 1)A \\ \mathcal{L}_i^r[A \cdot \min(1, 2G_i - 1)] + l_0 \cdot [(2G_i - 1)A - \alpha_i] & \text{if } \alpha_i < (2G_i - 1)A \end{cases}
\end{aligned} \tag{3}$$

where α_i is the suggested angle, A is the wave amplitude as in Eq. 2, and l_0 is the extra lengthening parameter that is fixed throughout this work (see Materials and Methods for more discussion). G_i is generalized compliance for the i -th joint, specifically in this work we maintain all joints to have the same generalized compliance value, i.e., $G_1 = \dots = G_N = G$.

This cable length control policy allows for programmable body compliance: as G increases, joints first become directionally (anisotropically) compliant due to the relaxation of one cable (Fig. 3B-i), i.e., L_i^l or L_i^r departs from \mathcal{L}_i^l or \mathcal{L}_i^r (Fig. 3B-ii). An emergent deployed angle ζ can depart from its suggested angle α in one specific direction (Fig. 3B-iii), i.e., a joint can admit forces to bend it further but reject forces from the other side. As a result, the projections of all feasible joint trajectories of ζ into the shape space yield a feasible region for gait paths to be perturbed by external forces, where the inner boundary is the ‘‘suggested’’ circular gait orbit (Fig. 3B-iv). As G further increases, joints become bidirectionally compliant due to the relaxation of the other cable (Fig. 3C-i), i.e., both L_i^l and L_i^r depart from \mathcal{L}_i^l and \mathcal{L}_i^r (Fig. 3C-ii). Thus ζ can then vary in both directions around α , i.e., a joint can admit forces from either sides (Fig. 3C-iii). The feasible region of gait path in the shape space correspondingly expands as the inner boundary shrinks (Fig. 3C-iv). Beyond one point ($G > 1.75$ in this work), the robophysical model becomes fully passive. Therefore, G works as a ‘‘knob’’ that we can tune to ‘‘program’’ how strongly the robophysical model is driven by the suggested shape, regulating the level of mechanical intelligence (Movie S2). Thus we can vary G in the robophysical model to investigate at which level of mechanical intelligence its locomotor performance can approach nematodes. A full schematic of properties that the robophysical model displays under different

G see Fig. S5.

Robophysical experiment verification of mechanical intelligence

To test the role of mechanical intelligence in limbless locomotion and its effect on locomotor performance, we conducted robophysical model experiments in four scaled-up environments (from open to dense) corresponding to the nematode study. In each environment, the robophysical model was under open-loop control, executing a suggested traveling-wave gait as in Eq. 2, with the shape parameters approximated directly from nematode kinematics in the corresponding environment so that the robophysical model used the same gaits as nematodes did. We varied G to access the locomotion displayed by the robophysical model in each environment. Quantifying locomotor performance (the wave efficiency η , the ratio of forward center of mass speed to backwards wave propagation speed) across the full range of G revealed that an appropriate G becomes necessary to facilitate open-loop traversal as heterogeneities arise (Fig. 4B). In flat terrain, η is inversely correlated to G . However, when obstacles were introduced, low G (≤ 0.5) resulted in frequent jams and becoming irreversibly stuck. At high G (≥ 1.5), the model failed to generate sufficient self-propulsion. $G = 0.75$ emerges as an appropriate G value for locomotion in all heterogeneous environments, as local maxima of η display at $G \approx 0.75$ (Movie S3). Further, η in the robophysical model with $G = 0.75$ increases as the obstacle density increases, well approaching η that displayed in nematodes (Fig. 4C).

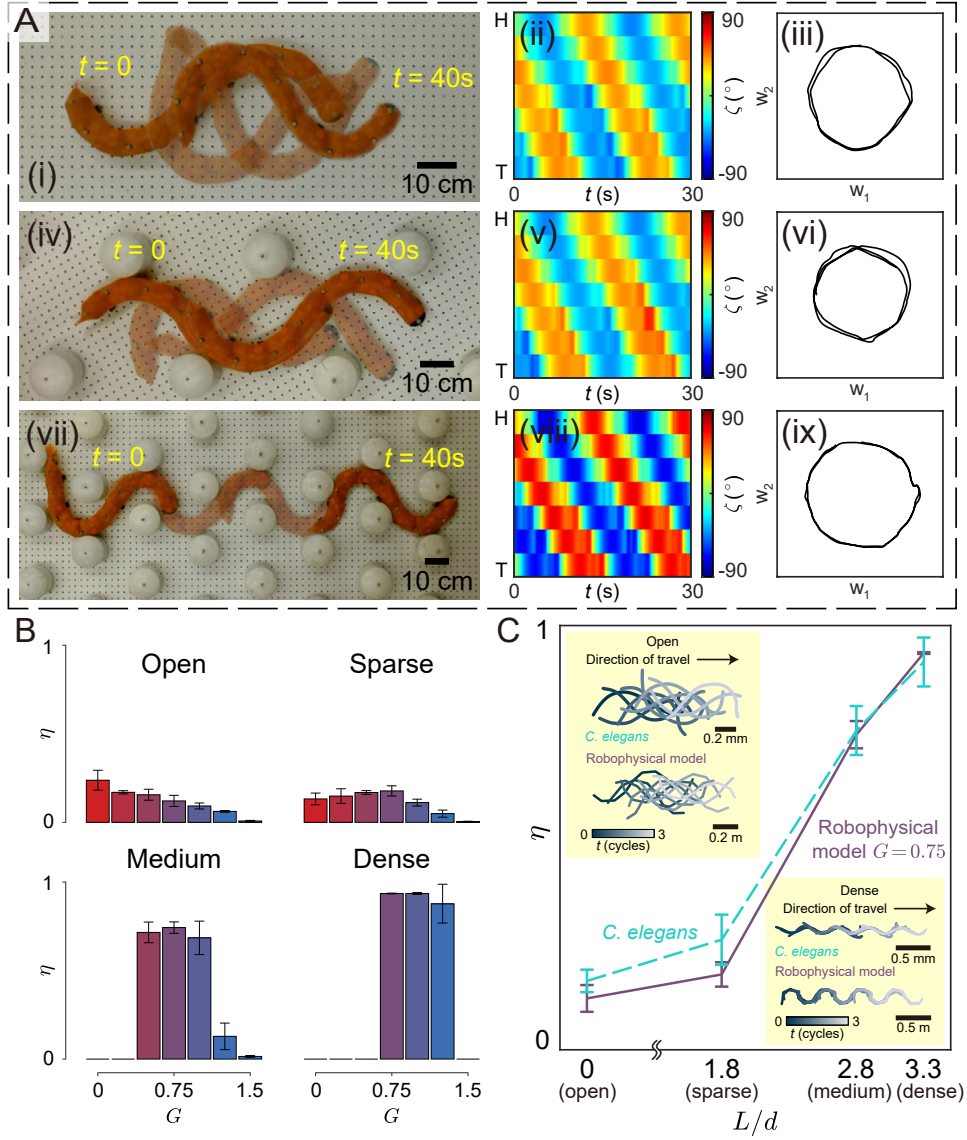


Fig. 4: Open-loop locomotor performance in the robophysical model that reveals the importance of mechanical intelligence in limbless undulatory locomotion. **(A)** Overlaid snapshots, emergent joint angles and gait paths in the shape space of robophysical locomotion ($G = 0.75$) in laboratory environments with varied obstacle density. **(B)** Locomotion speed (wave efficiency η) of the robophysical model as a function of generalized compliance G in environments with varied obstacle density (open, sparse, medium and dense). **(C)** Comparison of locomotion speed as a function of obstacle density between the biological model *C. elegans* and the robophysical model with $G = 0.75$, accompanied with example time traces of splined points along the body as the nematode and the robophysical model move in the open and dense environments (insets).

For $G = 0.75$ in the robophysical model, its body kinematics and gait orbits in shape space (Fig. 4A) closely resembled those observed in nematodes (Fig. 2A). The model performed an approximate traveling wave motion in flat terrain and sparser lattices, which resulted in nearly circular orbits in the shape space. In the dense lattice, analogous to the nematodes, we also observed small deviations from ideal travelling wave shapes, which converged quickly back to the circular orbit. Thus, the robophysical model serves as an effective model of nematode locomotion, well capturing both overall performance and detailed body kinematics (Movie S4).

The emergent match between *C. elegans* and the robophysical model kinematics and the enhancement of performance at $G = 0.75$ compared to other G values resulted completely from body compliance – simply by programmatically and anisotropically loosening the physical constraints on the joints in a way that mirrors the geometry of organismal patterns of activity, which allows joints to passively deform under external forces. Such a seemingly counter-intuitive result (improving performance via relaxing controls) verifies our hypothesis that the appropriate level of mechanical intelligence (purely passively, mechanically controlled emergent body-environment interactions) can facilitate heterogeneity navigation, and is sufficient to reproduce organismal lattice traversal performance.

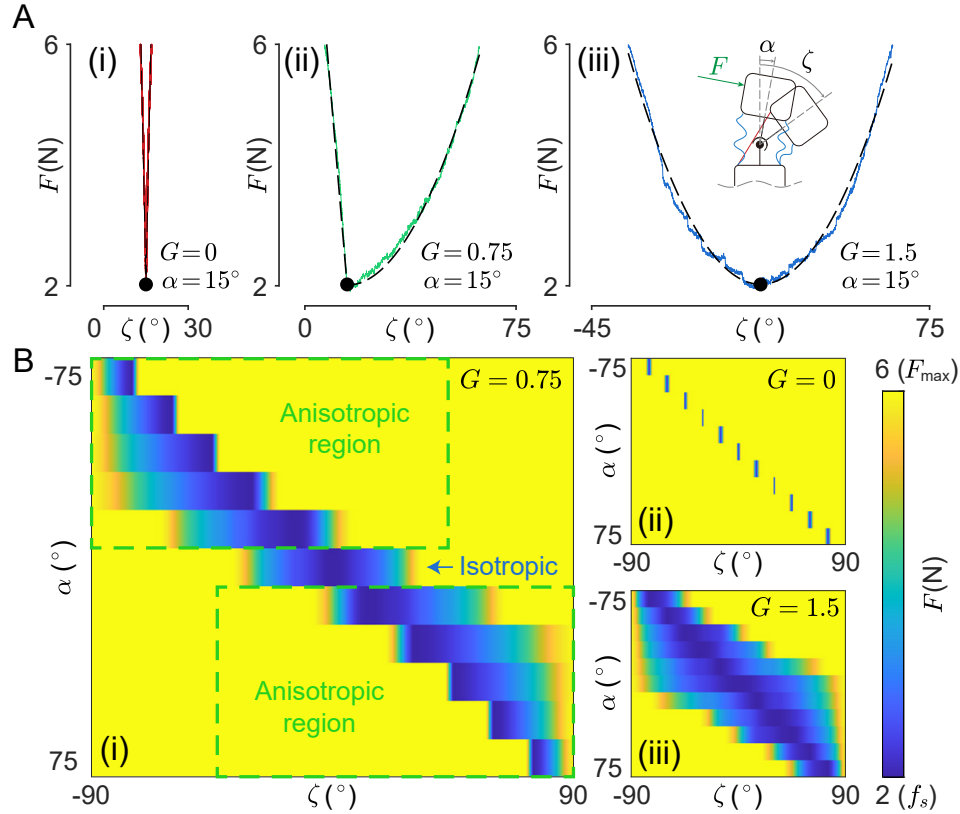


Fig. 5: Force-deformation characterization for mechanical intelligence in the body mechanism of the robophysical model. **(A)** External force versus emergent joint angle curves that show behaviors of a joint reacting to external forces under different compliance states. **(B)** Force-deformation maps of the robophysical model with varied G that show the robophysical model body properties can be programmatically tuned, thus working as a functional smart material.

Understanding mechanical intelligence via force-deformation characterization

we use the force-deformation properties of the robophysical model to identify how interactions with obstacles lead to deformations to the suggested traveling wave kinematics that enable successful lattice traversal. By characterizing the relation between the external force F and the emergent joint angle ζ at suggested angles α , we achieved maps of force-deformation properties of the robophysical model with varied G values (Fig. 5, for other G values see Fig. S8). For low

G , external forces produce minimal deformation of the joint for all parts of the cycle (unless they are sufficiently high to break the cable) (Fig. 5A-i, B-ii). While for high G , large deformations can be created in response to external forces in either direction (Fig. 5A-iii, B-iii). However, at $G = 0.75$, force-deformation responses become highly asymmetric at various points of the cycle (Fig. 5A-ii, B-i). For large angles, force is admitted in the direction of the bend but stiffly opposed in the opposite direction.

We hypothesize that this asymmetry allows the selective exploitation of thrust-producing interactions through rigid responses and deformations that prevent jamming in detrimental interactions, such as head-on collisions. Our robophysical model and many other limbless undulators move through space by passing body waves from head to tail with wave velocity v_{wave} anti-parallel to the center of mass velocity v_{CoM} (Fig. 6A). External forces F_{ext} from collisions that lie parallel to v_{wave} inhibit the center of mass motion, while collisions that produce forces parallel to v_{CoM} produce thrust. Fig. 6B shows the deflection from the suggested angle in response to a point force ($\approx 3N$) parallel or anti-parallel to v_{CoM} for a range of suggested joint angles at $G = 0.75$ (calculated using the force-deformation maps from Fig. 1E). At suggested joint angles with low amplitudes, deflection is permitted more symmetrically (i.e. $F_{\text{ext}} \parallel v_{\text{CoM}}$ and $F_{\text{ext}} \parallel v_{\text{wave}}$) produce a similar magnitude of deformation. However, as the amplitude of the suggested angle is increased, an asymmetry arises, producing an “easy” high compliance axis and “hard” high compliance axis. The direction of the easy and hard axes depends on the shape of the organism. When the “easy axis” is aligned with inhibitory interactions and the “hard axis” with thrust producing interactions, organisms can resist buckling while maintaining forward progress. Fig. 6C shows the orientation of the “easy”/high compliance direction (black triangles) and the “hard” low compliance (orange triangles) direction for 3 values of G (0, 0.75 and 1.5) and for the various joints along the body of an example 7-link undulator. Small arrows show point forces acting along the body either parallel to v_{CoM} or to v_{wave} . At $G = 0$,

all joints are symmetrically non-compliant, hence point forces produce either jamming interactions (small red arrows) or thrust (green red arrows). At $G = 0.75$ the distribution of easy and hard axes is arranged such that would-be jamming interactions are converted into body deformations which lead to bending and therefore successful obstacle traversal. At $G = 1.5$ all interactions permit substantial deformations (all joints are high compliance), while jamming is avoided entirely, there is no ability to produce coherent thrust.

This simplified model (Fig. 6) reveals that we can view the robophysical model as a programmable robotic “smart material” (52, 53) specialized for locomotion. For certain, intermediate values, of G , the robophysical model spontaneously converts inhibitory interactions into soft deflections while maintaining rigidity and thrust production in advantageous collisions without any explicit computation. The coordinated contraction and relaxation of the cables serves therefore not only to realize an approximate traveling wave body shape sequence, but also to dynamically modulate the material properties of the robot to buffer the motion to external collisions.

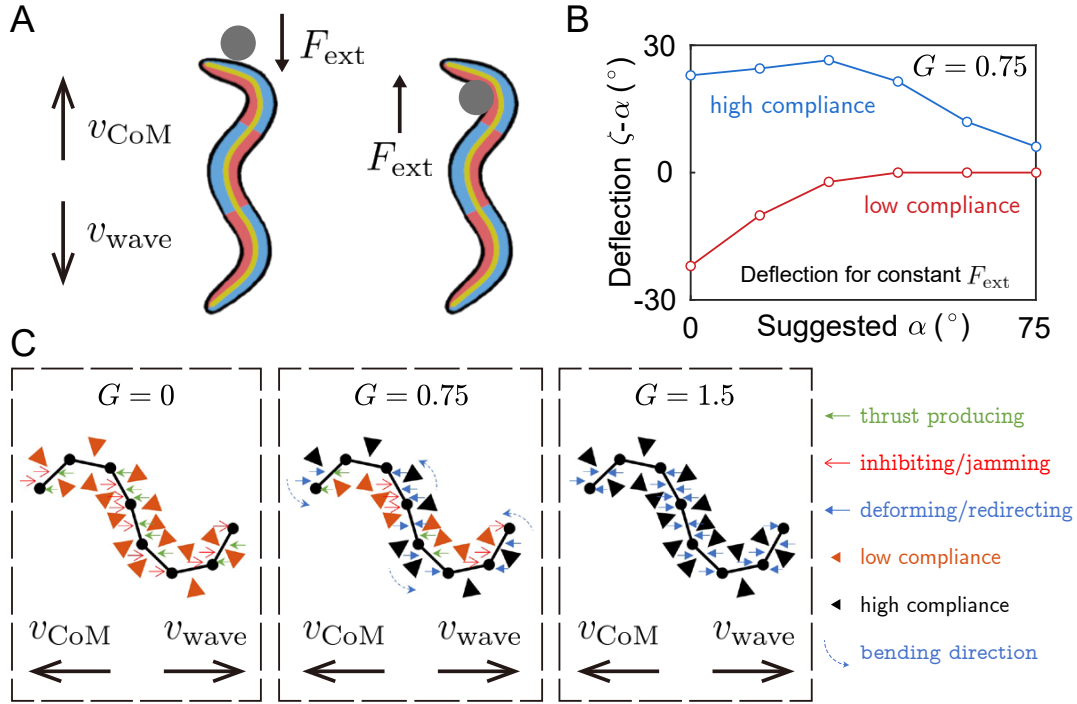


Fig. 6: A simplified model for understanding the functional mechanism of mechanical intelligence in limless locomotion. (A) Schematic illustration of an undulator facing inhibitory interactions (left) and thrust producing interactions (right). (B) Deflection angle in response to a point force F_{ext} either parallel or anti-parallel to v_{CoM} at $G = 0.75$ for different commanded angles, showing the response of the “easy” or high compliance direction and the “hard” low compliance direction. (C) The geometry of easy (black triangles) and hard directions (orange triangles) for a single posture across 3 representative values of G . Small arrows show point forces which are either thrust producing (green arrows), jamming (red arrows), or result in deformation of the undulator from the commanded shape (blue arrows) with bend directions indicated by the dashed blue lines.

Emergent correspondence of head behaviors in nematodes and the robo-physical model

The robo-physical model displayed emergent functional behaviors when $G = 0.75$. Upon collisions in the head, two typical head interaction events emerged in the robo-physical model to exploit the asymmetric force-deformation response: “gliding” where the head slides near-tangentially past the obstacle (Fig. 7A-i), and “buckling” where a collision induced a momen-

tary increase in the local curvature near the head, which then facilitated a shallower angle of attack (Fig. 7A-iii). Gliding leads to only minor deviations from circular paths in the shape space (Fig. 7A-ii), while buckling leads to larger deviations from the circular orbit, as the radius of the path increased at constant phase angle (Fig. 7A-iv). This transient cessation of the wave phase velocity arises as the obstacle restricts the forward progress, constraining the body and inducing increased curvature. Among all the events we collected ($N \approx 100$), we classified 33.6% as buckling (with a phase pause over 0.5 s) and other 66.4% as gliding. Given such behaviors take place in the open-loop robophysical model only commanded with a suggested traveling retrograde wave, the gliding and buckling behaviors instigated by collisions occur passively, and therefore are dominantly determined by passive body-environment interactions.

Given the correspondence on gross locomotor performance and body kinematics of the robophysical model and *C. elegans*, and the importance of head gliding and buckling dynamics in facilitating lattice transport, we next investigated if *C. elegans* displayed similar head (or neck) dynamics during obstacle interactions. Remarkably, we observed analogous behaviors (Fig. 7B-i to B-iv, Movie S5) such that 28.6% of head interaction events were classified as buckling (with a phase pause over 0.2s) while the rest were considered gliding ($N \approx 100$). We thus posit that the nematodes' head interactions help passively facilitate locomotion in heterogeneous environments, as manifestations of mechanical intelligence. Specifically, potentially inhibitory collisions that might lead to jamming are mitigated by the asymmetrical compliance in the head.

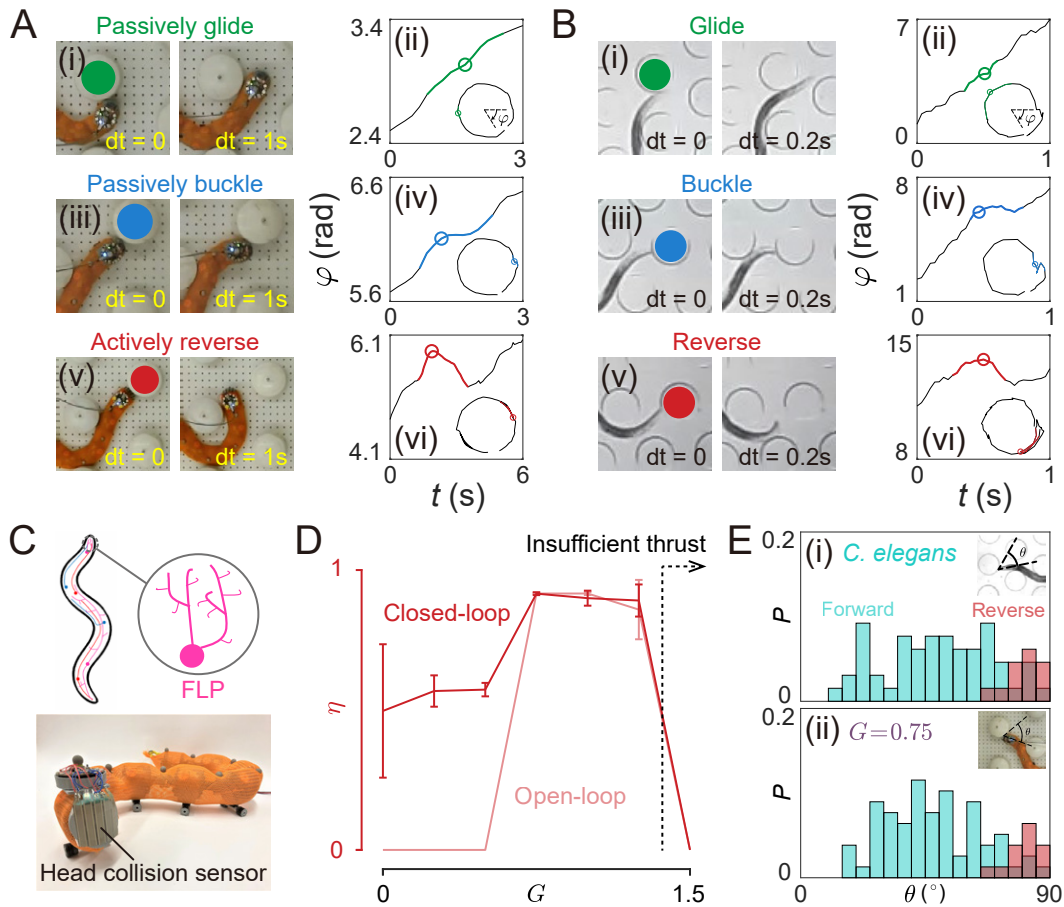


Fig. 7: Mechanical intelligence facilitates passive behaviors, and can be augmented via active behaviors. (A) The passive “gliding” and “buckling” behaviors, and an active “reversing” behavior in the robophysical model, along with their corresponding characteristic phase-time plots. (B) Analogous behaviors displayed by the biological model, along with corresponding phase-time plots. (C) The FLP dendrite sensory structure in nematodes, and the head collision sensor in the robophysical model for studying how reversals augment mechanical intelligence. (D) Wave efficiency as a function of G in the dense environment for the robophysical model with and without reversals, showing reversals can robustify robophysical locomotion. (E) Head collision angle probability distributions classified by post-collision motion directions (forward or reverse) in nematodes and the closed-loop robophysical model ($G = 0.75$).

Active reversals that exploit mechanical intelligence and enhance performance

Other than “gliding” and “buckling” head events, we also noted that in some instances *C. elegans* displayed a “reversal” behavior (Fig. 7B-v) correlated with collisions which we did not see in the open-loop robophysical model. The reversal behavior is an actively controlled behavior (54), in which nematodes initiate a reversal of the direction of the traveling wave for a short period, and then repropagate the original traveling wave (Fig. 7B-vi). We hypothesize that active responses to heterogeneities (even as simple as reversals induced by head collisions) could benefit locomotion by augmenting mechanical intelligence. The active reversals induced by high angle of incident collisions supplement mechanical intelligence by providing an alternative means of modulating the angle of attack. This reversal behavior is likely initiated by mechanosensory neurons in the head, such as FLP (Fig. 7C) which have stereotyped anterior cellular processes which likely transduce mechanical inputs into signals that produce the reversals (55).

Like theoretical and computational models in biomechanics, robophysical models allow tests of hypotheses that are inconvenient with living systems. Thus, we next used the robophysical model to probe possible functional locomotor roles of the active reversal behaviors positing that the inherent mechanical intelligence in the nematode could be augmented by simple head collision sensing feedback. To do so, we developed a head collision sensor (a force-sensitive resistor array, manufacturing and control details given in Methods) for the model (Fig. 7C) to allow real-time collision angle and force estimation. To realize reversal behavior, we programmed the device to reverse the direction of wave propagation when a harsh head collision (large collision force and angle) was detected.

We studied the dynamics of the closed-loop robophysical model with reversal capability in the dense environment and compared its locomotor performance to open-loop results. Reversals

enabled the robophysical model to traverse the environment in the low generalized compliance regime, which the open-loop strategy failed to (Fig. 7D, Movie S6), improving η in the range $0 \leq G \leq 0.5$. The reversal behaviors robustify the locomotion by increasing the range of G that allows the model to effectively locomote in the most challenging environment. The closed-loop robophysical model also showed remarkably similar kinematics as observed in nematodes (Fig. 7A-v, A-vi, Movie S5). Robophysical experiments revealed the function of reversal behaviors in undulatory locomotors: by not simply repeating the same movement back and forth in place, reversals allow the locomotor to take advantage of mechanically intelligent dynamics – passively adjusting body postures and spontaneously finding favorable position and orientation to generate effective thrust for locomoting further.

Given the similarity in behavioral kinematics between the closed-loop robophysical model and nematodes, we further investigated head collision angles and corresponding post-collision movement directions (forward or reverse) in both systems. The probability distributions of head collision angle for forward and reverse motion further demonstrate that the reversal-capable robophysical model with $G = 0.75$ well captures emergent behaviors that are induced by mechanical intelligence *C. elegans* (Fig. 7E, and probability distributions for other G values are shown in Fig. S6), thus works as a complete model of *C. elegans* locomotion (an example comparison of body kinematics see Fig. S7). Such qualitative agreement in body kinematics and the quantitative agreement in body event statistics imply that simple computational intelligence (reversals triggered by head sensing feedback) can compensate the short of mechanical intelligence (especially at low G region), or enhance mechanical intelligence (in terms of introducing extra chances for passive body-environment interactions), thus can augment locomotor performance. This also provides insight into the functional mechanism of the seemingly inefficient reversal behaviors displayed in nematodes. Our results also suggest that the spatiotemporal responses of the head sensory neurons such as FLP may be tuned to help facilitate obstacle navigation.

For instance the spatial structure of the cellular processes within the head (Fig. 7C) may produce allow the nematode to sense the collision angle, explaining the angular dependence of the different collision behaviors (Fig. 7E). Furthermore, the robophysical model demonstrates as a complete example of embodied intelligence (14, 16) and morphological computation (56, 57), displaying the most robust locomotion capabilities while working under the synergies of mechanical intelligence and computational intelligence.

DISCUSSION

In summary, our integrative and comparative study of biological and robophysical limbless locomotors reveals that mechanical intelligence, the general collection of emergent adaptive behaviors that arise from passive body-environment interactions, simplifies control in terrestrial limbless locomotion, especially in heterogeneous environments, and is sufficient to reproduce organismal lattice traversal performance. The robophysical model, once programmed with an appropriate level of compliance, not only accurately models undulatory organisms in terms of locomotor performance and body kinematics, but also in terms of dynamic force-deformation relationships (similar force-deformation relationships have been established for vertebrate undulators (58)). Dynamic force-deformation relationships are non-trivial for an organism of the scale of *C. elegans* (only passive viscoelastic properties have been determined for *C. elegans* (59)). Thus, our robophysical model is a useful tool for understanding the functional mechanism of mechanical intelligence in the organism – by identifying and understanding the mechanically intelligent control regimes of the robophysical model that accurately reproduce *C. elegans* kinematics in lattices, we can generate hypotheses about what underlying physiological and anatomical details are required to produce the emergent effective locomotion. Broadly, model organisms like *C. elegans* have an important role to play in connecting neural dynamics to behavior. Our results suggest that mechanics also play a significant role in shaping behav-

ior via processes that occur outside the nervous system, and therefore must be understood and accounted for to reach a comprehensive understanding of animal behavior in general.

Nematodes not only perform well in heterogeneous, collision-dominated environments. They also encounter a diverse array of substrates, including Newtonian fluids of varying viscosity and other flowable substances with complex, non-Newtonian rheologies (19). Hence, body compliance that enables lattice traversal, may also improve performance in less structured environments or, at a minimum not disrupt performance. We, therefore, hypothesized that our bilaterally actuated limbless robot would also display good performance without major changes in control in a diversity of robophysical model terrain with properties similar to those encountered during search and rescue and other applications. Indeed, we found that beyond functioning as a model for discovering and understanding emergent principles in limbless locomotion that cannot be directly tested with organisms, the bilaterally actuated limbless robot displayed unprecedented terrestrial mobility in diverse, complex, and more challenging environments.

We tested the robot in a range of environments (Fig. 8, Movie S7). Beyond regular lattices, the robot demonstrated effective traversal in randomly distributed obstacle terrains (Fig. 8A) and agile transitions from open terrain to obstacle terrain (Fig. 8B), where the robot was under open-loop controls with $G = 0.75$. Without the need for active adaptation of body shapes (35, 60, 61) or selection of paths (62–64) based on the awareness of internal states (e.g., instantaneous joint angles or torques) or knowledge of the surrounding environment (e.g., via contact sensing or visual feedback) as proposed in previous works, the mechanical intelligence in this robot enables compliant body-environment interactions, facilitating the spontaneous locomotion.

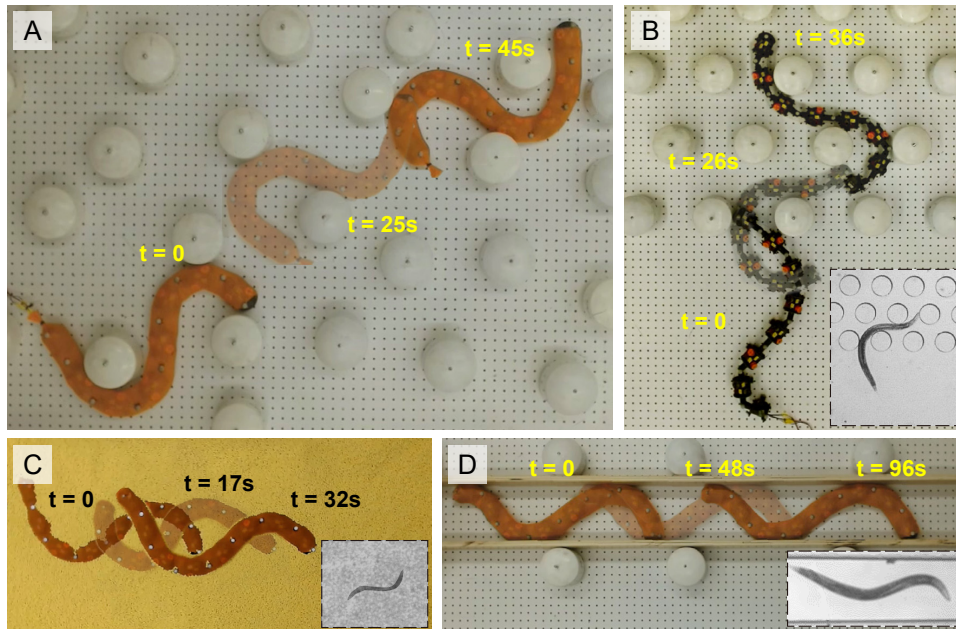


Fig. 8: Unprecedented open-loop robotic terrestrial capabilities in various types of complex environments facilitated by mechanical intelligence. (A) The robot traverses a randomly distributed obstacle array. (B) The robot transitions from flat ground to a densely distributed obstacle array, inset: *C. elegans* transitions from an open space to a dense lattice. (C) The robot locomotes in granular media (5 mm plastic spheres), inset: *C. elegans* locomotes in cryolites. (D) The robot moves in a narrow channel (18 cm width) formed with two parallel rigid walls, inset: *C. elegans* moves in a channel (65).

Further, we conducted tests of locomotion speeds and cost of transport in other types of environment, firstly granular media (Fig. 8C), a model flowable medium previously studied using other limbless systems (66, 67). In the granular material, we found that introducing an appropriate amount of passive body mechanics (by increasing G) can substantially reduce energy consumption without a remarkable loss of locomotor speed, with the local minimum in the cost of transport emerging at intermediate values of G (Fig. S9).

We also tested the robot in narrow channels which function as models of pipes (Fig. 8D), where we reversed the direction of the wave propagation to enable forward locomotion on the robot without wheels relying purely on wall interactions (see supplementary text for more dis-

cussion). The generalized compliance G enables spontaneous shape adaptation/modulation to a highly constrained channel without the need of probing the channel width in advance. And the local minimum of cost of transport emerged at high compliance $G = 1.25$. We also measured cost of transport in lattices with varied obstacle density (sparse, medium and dense as discussed previously), where we found local maxima of locomotion speed and local minima of cost of transport all emerged at intermediate values of G . For Detailed results of cost of transport and a further discussion see supplementary text.

Overall, intermediate values of G enable decent wave efficiencies in the largest range of environments, and provide reduced costs of transport (except for the flat ground). This suggests mechanical intelligence not only facilitates obstacle negotiation, but also can improve locomotion efficiency. Furthermore, because G can be dynamically tuned, we posit that adding sensory capabilities could enable the robot to choose the appropriate value of G for each particular environment to maximize energy savings or wave efficiency, effectively interpolating between shape control and compliant control.

In conclusion, the bilateral actuation scheme suggests a new design and control paradigm for limbless robots. Contrasting the lack of mechanical intelligence in limbless robots to date, the bilateral actuation mechanism offloads complex sensorimotor controls for handling body-environment interactions to mechanical intelligence, improving locomotion efficiency and freeing up onboard hardware and computational bandwidth for advanced sensing and motion planning techniques (36, 62, 68–75). This represents a paradigm shift in limbless robotics that could pave the way for the future development of more agile, intelligent and capable limbless robots that fulfill their promised potential of maneuverability in extremely complex environments, finding diverse applications such as search and rescue, industrial inspection, agricultural management, and planetary exploration.

MATERIALS AND METHODS

Biological Experiments

Wild-type *C. elegans* (QLN2) was used for all experiments. Nematodes were cultured using standard protocols on NGM agar plates with *Escherichia coli* (OP-50) lawns. Nematodes were cultured at 20°C and synchronized to day-1 adults for all studies.

Micro-fluidic pillar arrays were constructed using conventional soft-lithography techniques (Fig. S1A). SU-8 molds were patterned via UV photolithography. Polydimethylsiloxane or PDMS (Dow Corning Sylgard 184) was poured onto the molds (10:1 elastomer to curing agent ratio), cured at 70°C overnight in an oven and peeled from the molds. The PDMS devices were cut into shapes and holes for nematode loading and fluid flow were punched using a biopsy punch. Devices were then bonded to glass substrates using a handheld corona plasma treatment wand.

Microfluidic devices were first degassed using by flowing in a Pluronic and DI water mixture. Once all air was removed, the devices were flushed with flowing S-basal buffer for several minutes. Nematodes were then loaded rinsed off of their plates with S-basal, washed 3 times and loaded into a syringe. The syringe was then connected to the device and nematodes were pushed into the pillar array. The device was then sealed using capped syringe tips in the entry and exit ports and then continuously imaged for 10 minutes at 20 FPS on a dissecting scope (Leica).

Biological Data Processing

Video recordings were first cropped to isolate bouts of individual nematodes performing crawling behaviors (stationary nematodes were ignored). A reference image containing only the pillars was constructed by averaging the frames of an entire bout, or by selecting a frame when the nematode was out of the cropped video. Background subtraction was then performed to isolate

the nematode. Thresholding was used to binarize the image of the nematode, creating a series of black and white masks. Each mask was then skeletonized to isolate the centerline. These image processing steps were performed in ImageJ. The centerlines were then converted into curvature heatmaps in MATLAB, using a B-spline to interpolate between the pixel-wise centerline points. The curvatures were then used to perform subsequent analysis using MATLAB.

To simplify the analysis of locomotion kinematics in lattices, we exploit dimensionality reduction techniques. Prior work illustrated that the majority of body postures in undulating systems can be described by linear combinations of sine-like shape-basis functions, despite the inherently high dimensionality of postural data (47, 48). We assume that the essence of the body-curvature profile κ at time t and location s ($s = 0$ denotes head and $s = 1$ denotes tail) can be approximated by Eq. 1, where ξ is the spatial frequency of body undulation obtained from direct fitting. $w_1(t)$ and $w_2(t)$ are the reduced shape variables describing the instantaneous shape of the locomotor at time t . Thus, the locomotion may be visualized as a path through a two-dimensional “shape space” defined by w_1 and w_2 . Practically, we first performed principal component analysis to the curvature data ($\kappa(s, t)$) to extract the first two principle components, which account for over 85% of the variation in observed body configurations. Then we fitted two shape-basis functions, in the form of $\sin(2\pi\xi s)$ and $\cos(2\pi\xi s)$, to the principle components (Fig. S2). We projected the curvatures onto the shape-basis functions, by finding the least-squares solution (76), to extract the weights of shape-basis functions, i.e., shape parameters, $w_1(t)$ and $w_2(t)$. The gait path then is the trajectory formed by $w_1(t)$ and $w_2(t)$ in the shape space spanned by w_1 and w_2 .

Collision events with pillars were identified manually, and the angle of the head and the pillar were calculated manually in ImageJ. To calculate wave efficiencies, bouts of locomotion containing at least 3 cycles of forward movement were selected. The wave efficiency is calculated as $\eta = v_{\text{CoM}}/v_{\text{wave}}$, where v_{CoM} is the center of mass velocity of the organism and v_{wave} is

the wave speed. v_{CoM} was calculated directly from microscopy videos using the distance traveled by the nematode's head over an integer number of wave cycles. The wave speed $v_{\text{wave}} = f\lambda$ was calculated using the measured frequency and wavelength of each nematode. For the head collision angle of nematodes, we measured the angle between the body centerline and the tangential line of the pillar that passes the contact point. To classify gliding and buckling in the collection of head collision events which followed with forward body movement (no reversal), we examined the nematode body kinematics and calculated phase over time around the collision time. we classified the events that led to a phase pause over 0.2 second as buckling while others as gliding.

Robophysical Model Design and Manufacturing

The robophysical model was constructed as a chain of linked identical modules (Fig. S3, 7 joints and 86 cm body length). Each individual module consisted of a two-axes servo motor housed inside a case. The cases were attached to one another with a unilaterally bending joint linkage. Pulleys were then attached to each axis of the motor, and the pulleys were spooled with strings, which were referred to as cables. To complete the design, the cables were unspooled through the case and fixed onto the case ahead of the current one. Additional add-on features, such as skins and wheels, were also included for specific robophysical experiments to model the biological model.

Each module contained a Dynamixel 2XL430-W250-T servo motor (ROBOTIS), which had two axes that could be controlled independently. This feature enables the left and right cables to be adjusted to different lengths as needed. With a stall torque of 1.4 Nm, the motor provides ample support for the cable tension resulting from body-environment interactions. Additionally, the motor offers precise and continuous position control, with small enough resolution for multiple rotations. This feature allows for accurate cable length controls, where it is assumed that

the cable length was approximately proportional to the motor position within the range between the maximum and minimum cable lengths.

The case that houses the servo motor serves as the main structural component and skeleton of the body. It was custom designed (55 mm length, 68 mm diameter) and manufactured to fit the motor's geometry and was 3D printed (Raise3D E2 3D printer) using PLA material. To attach the case to other components, such as the joint and wheels, heat-insets were inserted into all the holes. All the cases were identical, except for the one at the anterior end (head) of the robophysical model, which had a rounded shape for smoother head-obstacle interactions.

The joint (28 mm length) connecting adjacent modules in our system provides one degree of freedom rotation, with the axis of rotation perpendicular to the ground surface. We 3D printed joints with PLA material. Each joint allows a full range of 180 degrees of rotation, from -90 to $+90$ degrees, with the neutral position at 0 degrees where the two links align. The joints are secured to the cases with two screws that connect directly to the heat insets, facilitating easy rearrangement and replacement.

The cables are the component that drives the movement of the robophysical model. To achieve this, we utilized nonelastic fishing lines (Rikimura) that boast high tensile strength of up to 180 pounds and demonstrate negligible deformation and shape memory upon stretching. To control the contraction and relaxation of the cables, we employed pulleys (15-mm diameter) that were 3D printed using PLA material and attached to each rotational shaft of the servo motor. One end of each cable was fixed to the pulley, while the rest was tightly wound around it. This configuration allows the length of the cable to vary proportionally with the rotation angle of the pulley, which can be accurately controlled by the servo motor. The other end of each cable was threaded through a small guiding hole on the edge of the case and attached to the other case linked by the joint. For each joint, two cables were present on either side, controlling the full range of motion of the joint. A cable contracts when it is taut and under tension, while it relaxes

when it is slack and has no tension.

Our robophysical model was controlled using code developed with the Dynamixel SDK library and programmed in MATLAB. Control signals were transmitted to the robophysical model from a PC via U2D2 (ROBOTIS). We powered the motors using a DC power supply (HY3050EX) with a voltage setting of 11.1 V. As the servo motors were connected in a daisy chain configuration for both power and communication, we connected the U2D2 and power supply to the last motor in the series.

The skin used on the robophysical model in experiments was an elastic mesh sleeve (1.75-inch ID polyester fabric expandable sleeving, McMaster-Carr) that wrapped around the robophysical model body. Note that the skin cannot create anisotropy to provide any extra propulsion. The benefit of using an isotropic skin is twofold. The robophysical model is made of hard modules and joints, it therefore can get wedged unexpectedly in the heterogeneities because of the irregular structures, such as edges of the case. The skin thus guarantees smooth body contact with the environment. The skin also provides weak passive elasticity, facilitating a weak but inherent “potential” for the robophysical model to return to the straight position. This elasticity was found helpful especially in the passive behaviors that the robophysical model displayed and share similarity with those in biological model. The force effect of the skin was also considered when the force-deformation properties of the robophysical model were characterized.

The wheels are attachable components that can be attached or removed from the bottom of each case. To attach wheels onto the case, a base was 3D printed using PLA and screwed to the base. Then, the wheel frame (LEGO) was screwed into the base. To achieve a similar drag anisotropy for the robophysical model as for the biological model ($\sim 2 : 1$), we replaced the rubber tires with low-friction fiberglass tape (McMaster-Carr), resulting in a 1.6 : 1 drag anisotropy ($F_{\perp}/F_{\parallel} = 1.6/1$, verified with wheel force experiments following the protocols proposed in (77)). This allowed for a better comparison of the performance of the robophysical

model and the biological model. Noted that in open and sparse environments, wheels are necessary for the robophysical model to produce propulsion with drag anisotropy. However, as heterogeneity density increases, the propulsion forces provided by pushing off heterogeneity generally dominates the locomotion, and the robophysical model can move forward effectively without wheels. For consistency in the experimental setup and comparison with the biological model, we kept the wheels on for robophysical experiments in all environments.

The head collision sensor is an add-on structure in the closed-loop robophysical model, for studying how mechanical intelligence can be imposed by active reversal behaviors and modeling the head sensing neurons of *C. elegans*, we designed and 3D printed a head for the robophysical model that is capable of sensing the collision angle (discrete) and the rough magnitude of collision forces. Five force-sensing resistors (FSR, Interlink Electronics FSR Model 408) were attached in parallel on the curved head surface (Fig. 7C). The feedback analog signals were collected using an Arduino micro-controller (Seeeduino XIAO SAMD21). The collision angle ranges that each FSR can detect are roughly 65° to 75° , 75° to 85° , 85° to 95° , 95° to 105° and 105° to 115° . The thresholds that we set to trigger the reversal behavior in the closed-loop control of the robophysical model were 3 N for the 3rd FSR (the middle) and 5 N for the 2nd and 4th FSR (left and right middle). When the head collision sensor sensed collision force beyond the set thresholds, the robophysical model was programmed to initiate a reversal behavior, where we fixed the reverse duration to be 0.125 cycle so that we focus on studying the effect of reversals, despite that the duration of nematode reversals was observed to vary from 0.1 to 2 cycles.

Robophysical Model Control

We calculated the exact lengths of the left and right cables that can form a joint angle α , $\mathcal{L}^l(\alpha_i)$ and $\mathcal{L}^r(\alpha_i)$, based on the geometry of the joint mechanical design (Fig. S4). “Exact length”

means the cable is in a contracted state, forming a straight line. Thus, \mathcal{L}^l and \mathcal{L}^r follow

$$\begin{aligned}\mathcal{L}^l(\alpha_i) &= 2\sqrt{L_1^2 + L_2^2} \cos \left[-\frac{\alpha_i}{2} + \tan^{-1} \left(\frac{L_1}{L_2} \right) \right], \\ \mathcal{L}^r(\alpha_i) &= 2\sqrt{L_1^2 + L_2^2} \cos \left[\frac{\alpha_i}{2} + \tan^{-1} \left(\frac{L_1}{L_2} \right) \right].\end{aligned}\tag{4}$$

Considering design parameters of our robophysical model, we have

$$\begin{aligned}\mathcal{L}^l(\alpha_i) &= 79.2 \cos \left(-\frac{\theta_i}{2} + \frac{\pi}{4} \right) \text{ mm}, \\ \mathcal{L}^r(\alpha_i) &= 79.2 \cos \left(\frac{\theta_i}{2} + \frac{\pi}{4} \right) \text{ mm}.\end{aligned}\tag{5}$$

We followed Eq. 3 to control the lengths of the left and right cables $L_i^{l/r}$ for the i -th joint. We converted the linear motion of contracting and relaxing cables to the rotary motion of pulleys by spooling cables onto them. Since arc length is proportional to the center rotational angle, which we can directly control via servo motor (4096 positions per full rotation, 0.088° resolution), we commanded the motor position P to achieve the shortening and lengthening of cable length L using

$$P(L) = P_0 + \gamma L,\tag{6}$$

where P_0 is the position of the motor when the cable length is 0 (calibrated for each cable), and $\gamma = -\frac{360 \text{ (}^\circ \text{ per full rotation)}}{\pi D_{\text{pulley}} \cdot 0.088 \text{ (resolution)}} = -86.8 \text{ mm}^{-1}$. Note that $L \geq 0$ and we regulated the positive direction of motor rotation corresponds to the contraction of the cable, according to our mechanical design, thus P_0 is the maximum motor position and γ is negative. Also note that, we neglected the change of pulley radii due to the thickness of the cable ($< 0.5 \text{ mm}$). By substituting Eq. 3 into Eq. 6, we obtained the control policy in terms of motor position that we directly programmed to run the robophysical model. Practically, we set γl_0 to be a constant with a magnitude of 100 throughout this work, yielding $l_0 = 1.15 \text{ mm}^\circ$.

By varying the value of generalized compliance G , the robophysical model can display different levels of body compliance and mechanical intelligence, allowing the robophysical model

to implement specific kinematics (e.g., gaits from nematodes) while passively mediate and respond to environmental perturbations passively. Fig. S5 provides a detailed explanation of the behaviors that one single joint and the whole robophysical model can display when G falls in different ranges. The first schematic in each row shows the state of the joint (either bidirectionally non-compliant, directionally compliant, or bidirectionally compliant) and the state of left and right cables (either contracted or relaxed) depending on which region the suggested joint angle falls into. The second plot in each row illustrates the actual (deployed) lengths comparing with the exact lengths of left and right cables on either sides of the joint as a function of the suggested joint angle, where overlaps of actual and exact lengths means the cable is contracted, while the discrepancy between actual and exact lengths shows how much the cable is relaxed. Note that $\mathcal{L}(0)$ on the y-axis means the exact length of a cable when joint angle is 0, \mathcal{L}_{\max} and \mathcal{L}_{\min} mean the exact length of the left (right) cable when the joint angle is 90° and -90° (-90° and 90°), respectively. The third plot in each row illustrates the feasible range of all possible emergent, deployed joint angle, showing how much a single joint angle could depart the suggested joint angle by perturbation of external forces, enabled by relaxation of cables. The last figure in each row depicts the feasible region of all possible emergent, deployed gait paths of the robophysical model, taking all joints as a whole, in the shape space spanned by w_1 and w_2 . We projected the collection of upper bounds for all joints onto the \sin and \cos shape bases to acquire the outer bound of the possible gait paths. And similarly we projected lower bounds of joint angle to acquire the inner bound of the possible gait paths. The region bounded by inner and outer bounds then illustrates how much the robophysical model could depart the suggested gait path by perturbation of external forces.

Robophysical Experiments

We built laboratory models of heterogeneous terrains (Fig. S1B) scaled to the dimensions of the robot, comparable to those used in biological experiments. The wheels coated by low-friction fiberglass tape that were equipped on the robophysical model can create a $\sim 1.6:1$ drag anisotropy, which is close to that for nematode in the liquid between pillars, assumed to be modelled by a cylindrical cross section in a low-Re viscous fluid (78, 79). Note that, the magnitude of reaction force on wheels of the robophysical model is speed independent (77), while the magnitude of reaction force is linearly dependent on speed for nematodes in viscous fluid. However, drag anisotropy is the dominant factor in governing performance in undulatory locomotion (80), and the difference between frictional and viscous drag are likely to be subtle. Finally, we fixed the suggested gait parameters for the robophysical model and the spacing between obstacles in the model heterogeneous terrains, such that locomotion displayed by the biological model and the robophysical model share the same wavelength-spacing ratio (~ 2 for the sparse environment, ~ 2.2 for the sparse environment, and ~ 1.8 for the dense environment, approximated from biological locomotion data).

Environment Setup

The robophysical experiments were conducted on a level pegboard (The Home Depot) measuring 2.4 meters in length and 1.2 meters in width, with 6.35-mm holes spaced at every 25.4 mm. Each hole has screw inserts that are fitted for 4-mm bolts that can be used to secure PVC pipe caps. The pipe caps (Charlotte, 12.7 cm in diameter and 10 cm in height) were used as reconfigurable obstacles in the experiments. They have 4-mm holes drilled at their center and can be secured to the pegboard using long 4-mm bolts (McMaster-Carr) that were fastened into the screw inserts. An example lattice configuration is shown in Fig. S1B. This experimental setup allows for obstacles to be easily rearranged and spaced on the pegboard to match the pillar

spacings of different lattices in the nematode experiments.

The OptiTrack motion-tracking system was utilized to record the positions and postures of the robophysical model in the workspace. Six IR cameras (OptiTrack Flex 3) were mounted above the lattice to capture the real-time 3D positions of nine reflective markers attached to the robophysical model's body, including seven at each joint, one at the anterior end, and one at the posterior end. The X, Y, and Z position values of each marker were obtained from the Motive software using MATLAB. In addition, a high-resolution camera (Logitech HD Pro Webcam C920) was mounted above the experiment environment to record videos of each experiment. The footage was used to analyze the head collision angle probability distributions classified by post-collision motion directions.

Experiment Protocol

Robophysical experiments consisted of a series of trials running the robophysical model in the lattices. One trial was running the robophysical model from an initial position until it reached an end state. The end states occurred because of one of the following conditions: 1) the robophysical model reached the boundary and exits the lattice, 2) the robophysical model was stuck (did not proceed for 10 consecutive gait cycles) or 3) the servo motor stopped working because of overloading (experiencing torque that exceeded its stall torque). Three separate trials were conducted for each generalized compliance value (ranging from 0 to 1.5 with a 0.25 interval) in each of the four environments (open, sparse, medium, and dense). To ensure consistency across trials, three initial positions were randomly selected and kept identical for all values of generalized compliance.

The methods for the calculation of wave efficiency and the measurement of head collision angle in the robophysical model are the same as nematodes, based on tracked data. The method for classification of the passive behaviors is the same as well, while the threshold of phase

pauses for buckling classification was 0.5 second for the robophysical model.

Force-Deformation Characterization Experiment

Force-deformation experiments were performed by measuring the relation between the magnitude of an external pushing force exerted on an joint with a certain G and the emergent deployed joint angle. We designed a custom, 3D printed stick to push the robophysical model. The stick was attached to a load cell (FUTEK LLB350-FSH03999), and the load cell was mounted the force sensor to a robot arm (DENSO VS-087), as shown in Fig. S8A. The robot arm was programmed to move the stick in a circle at a constant 1 mm/s velocity, where the center of the circle was colinear with the rotation axis of the joint and the radius of the circle was 60 mm such that the pushing point was at the middle of the module. Analog signals of the load cell were passed through an analog amplifier (FUTEK IAA100), then an analog to digital multifunctional data acquisition module (NI USB-6009), and the digital signal was recorded using NI LabVIEW. The robot body was fixed to a rigid table using two wooden planks that are firmly secured to the table. The robot is pinched between the planks, fixing it to the table surface. One single robot joint is left extending out past the planks for the force-deformation experiments. The joint is given a specified joint angle and G value before the start of the experiment. Specified angle values were swept from -75° to 75° with a 15° increments.

In each experiment, the end effector of the robot arm began rotating from the suggested angle until the force reaches a maximum value, set as 6 N which is sufficiently large to bend a compliant joint but would not break the robophysical model. And this process was repeated in the clockwise direction starting from the suggested angle. Taking all force-emergent angle characterizations together, we show maps of force-deformation properties with varied G (Fig. S8B), showing the robophysical model as a programmable functional smart material.

Acknowledgments

The authors would like to thank Zhexin Shen for the help with manufacturing the head collision sensor, Valerie Zborovsky and Zach James for their help with robophysical and biological experiments, Lucinda Peng for useful discussions, and Daniel Soto for the help with construction of robophysical experiment environment.

Supplementary Materials for Mechanical Intelligence Simplifies Control in Terrestrial Limbless Locomotion

Tianyu Wang *et al.*

*Corresponding author: Daniel I. Goldman, daniel.goldman@physics.gatech.edu

Supplementary text

Supplementary results and discussion of robot performance in diverse environments

Evaluation metrics and methods

In addition to the wave efficiency η (which is the ratio of the center of mass velocity to the wave propagation velocity) that we used to describe the robot's locomotion speed, we also calculated the mechanical cost of transport c_{mt} . This dimensionless quantity, widely used in the study of legged animals and robots (26, 81–83), gives the work required to move a unit body weight a unit distance and allows us to analyze the robot's locomotion efficiency in a more comprehensive manner.

To calculate the mechanical cost of transport, we used the formula $c_{\text{mt}} = W/mgd$, where W is the work done by cables, mg is the robot's weight, and d is the distance traveled. We estimated the tension T exerted by each cable using the torque sensor embedded in the servo motor (ROBOTIS 2XL430-W250-T). During an experiment, we recorded the torque readings τ from the motor with a time interval of $\Delta t = 10$ ms. To obtain the nominal torque readings τ_0 , which represent the "metabolic" torques required to enable the shaft to rotate without moving the robot, we ran a calibration experiment with the same motor running the same trajectory without tying the cable to the pulley. We then estimated the tension at each time step using the formula $T = (\tau - \tau_0)/R_{\text{pulley}}$, where R_{pulley} is the radius of the pulley (see Materials and

Methods). To estimate the distance traveled Δl , we measured the rotation angle difference $\Delta\beta$ of the servo motor via its internal encoder within the time interval Δt times R_{pulley} . By summing up the products of the tension and distance for each time step, we calculated the work done by one cable during an experiment. We then summed up the work done by all cables to obtain the total work done by cables. The traveled distance d was measured using tracking data by summing up the distance traveled by the robot’s center of geometry during each time interval.

Flat ground

Fig. S9A shows the robot’s wave efficiency η and mechanical cost of transport c_{mt} on a wood-surface flat ground, where the robot was equipped with wheels to generate a $\sim 1.6:1$ drag anisotropy and move forward with retrograde wave propagation along the body (see Materials and Methods). Gait parameters were fixed as $A = 46^\circ$ and $\xi = 0.81$ as discussed in Materials and Methods. As the generalized compliance G increases, we observed a nearly proportional decrease in η and increase in c_{mt} . We omitted data points where $c_{\text{mt}} > 20$ in all the plots. The robot’s performance on the flat ground serves as a benchmark for comparison with other environments that we tested.

Granular media

As demonstrated in previous work, a limbless robot can generate forward thrust in granular media with retrograde wave (66, 84), thus the robot was not equipped with wheels for tests in granular media. The experiments were conducted in a pool of plastic spheres with a diameter of 5 mm, which could not enter the motor and potentially damage the robot. Gait parameters were fixed as $A = 60^\circ$ and $\xi = 1$. At the range of $0 \leq G \leq 1$, η shares a similar decreasing trend as on the flat ground (Fig. S9B). Surprisingly, we observed a more dramatic decrease in the work done by cables, yielding a decreasing c_{mt} with a local minima at $G = 0.75$. From this result we posit that, with lower body compliance, much of the active work done by the robot

cannot effectively transfer into thrusting forces in such environments, and is wasted instead. By increasing the body compliance to let the robot “flow” with the environment (react to it), we reduce energy consumption without sacrificing locomotion speed. However, when G is too high, the locomotion speed drops significantly, leading to an increase in c_{mt} . Such result suggests that by leveraging the mechanical intelligence in locomotion, the robot has the potential to move efficiently within granular media.

Channel

Channels were set up to function as models for pipes and other environments where body shapes of the robot in lateral direction are highly constrained. Previous work has modeled and demonstrated that a limbless robot can gain thrust forces purely from its interactions with walls without the need of wheels for creating drag anisotropy (67). Differing from nematodes using retrograde waves to move in channels (65, 85) where we posit their thrusts primarily result from the drag anisotropy of the fluid interactions, the robot with isotropic friction needs to use direct waves to produce forward motion, solely through forces experienced on the wall. In our experiments, the robot was not equipped with wheels and we commanded the robot with a direct wave (change “-” into “+” in Eq. 2) with parameters $A = 60^\circ$ and $\xi = 1$. Specifically, the width of the robot body while employing this gait was measured as 23 cm. To make the channel a challenging environment, we set the width of the channel as 18 cm such that the robot need to “squeeze” its body to adapt to it, which is usually the case in applications such as pipe inspection. As a result (Fig. S9C), our robot cannot fit into the environment until $G = 1$. When $G \geq 1$, the robot generated effective forward locomotion in the channel and the local minima of c_{mt} emerged at $G = 1.25$. This result suggests that the generalized compliance G enables spontaneous shape adaptation to the channel for without the need of probing channel width in advance, and reduced c_{mt} meanwhile. Notably, this conclusion holds true even for a wheeled limbless robot

employing a retrograde wave with drag anisotropy.

Lattice

In addition to η that has been reported in the main text for the robot in regular lattices with varied density of obstacles, we evaluated c_{mt} for all experiments (Fig. S9D to E). As introduced in Materials and Methods, the robot was in the same condition as in experiments on the flat ground (with wheels), and executing open-loop gaits with fixed parameters obtained from direct fitting from nematode kinematics in biological experiments.

Firstly, the obstacles in the sparse lattice impede locomotion of the robot with low G , resulting in reduced η compared to that on the flat ground. However, with an increasing G , the more compliant robot emerged to utilize the obstacles to generate thrust by pushing off of them, leading to an improved η , known as obstacle-aided locomotion. The local minimum of c_{mt} emerged at $G = 0.75$, where we observed both increased locomotion speed and decreased energy consumption compared to lower G values.

In the medium lattice, the robot started to become “stuck” on obstacles, where the robot cannot traverse the lattice with the commanded gait while the body was relatively rigid ($G = 0$ and 0.25). However, under the same open-loop control for the basic pattern of head-to-tail wave propagation, locomotion emerged when the body was more compliant, where η and c_{mt} also reached their maximum and minimum in the range of $0.5 \leq G \leq 1$. While when the body is too compliant ($G > 1$), the robot cannot generate sufficient thrust, leading to a dramatic drop in η and increase c_{mt} .

In our experiments, we observed a similar result in the dense lattice, where only intermediate values of G led to effective and efficient locomotion. Interestingly, we also noted a slight shift in the effective range of G from $0.5 \leq G \leq 1$ (medium lattice) to $0.75 \leq G \leq 1.25$ (dense lattice). We posit that, with lower G values, the robot is better able to generate thrust

by utilizing drag anisotropy, but may struggle with adapting to the environment. On the other hand, with higher G values, the robot is more compliant to the environment, but may have reduced capabilities for generating thrust (as also demonstrated by the flat ground data). As the obstacle density increases from medium to dense lattice, the constraints on body shapes become stronger, requiring the robot to be more compliant. On the other hand, in such environments, the contact forces between the robot body and the obstacles play a more dominant role in the robot's forward motion, surpassing the contribution of drag anisotropy (as evident from the robot's ability to move in the dense lattice without wheels). Therefore, higher values of G are preferred in denser lattices, which explains the slight shift in the effective range of G from the medium lattice to the dense lattice.

Discussion

In summary, our findings indicate that in highly constrained environments where interactions between the robot body and the environment play a dominant role in locomotion, an intermediate range of generalized compliance ($0.75 \leq G \leq 1.25$) enables the robot to be compliant enough to adapt to the environment, while minimizing the work required to maintain the wave propagation pattern. This results in local minima of c_{mt} , indicating an optimal balance between compliance and wave propagation efficiency. This insight sheds light on the importance of generalized compliance in enabling effective locomotion in challenging environments such as non-movable obstacles in medium/dense lattices and channels, where the robot needs to adapt its body shape to the environment while minimizing energy expenditure.

Supplementary Figures

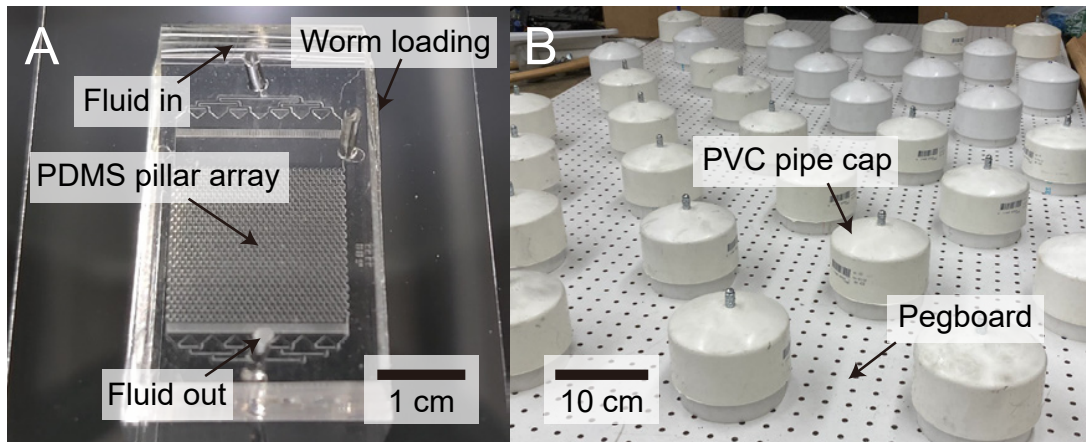


Fig. S1: Heterogeneous environments for investigating mechanical intelligence in limbless locomotor. (A) A microscopic pillar array for studying locomotion of *C. elegans*. (B) A macroscopic obstacle terrain for studying locomotion of the robophysical model.

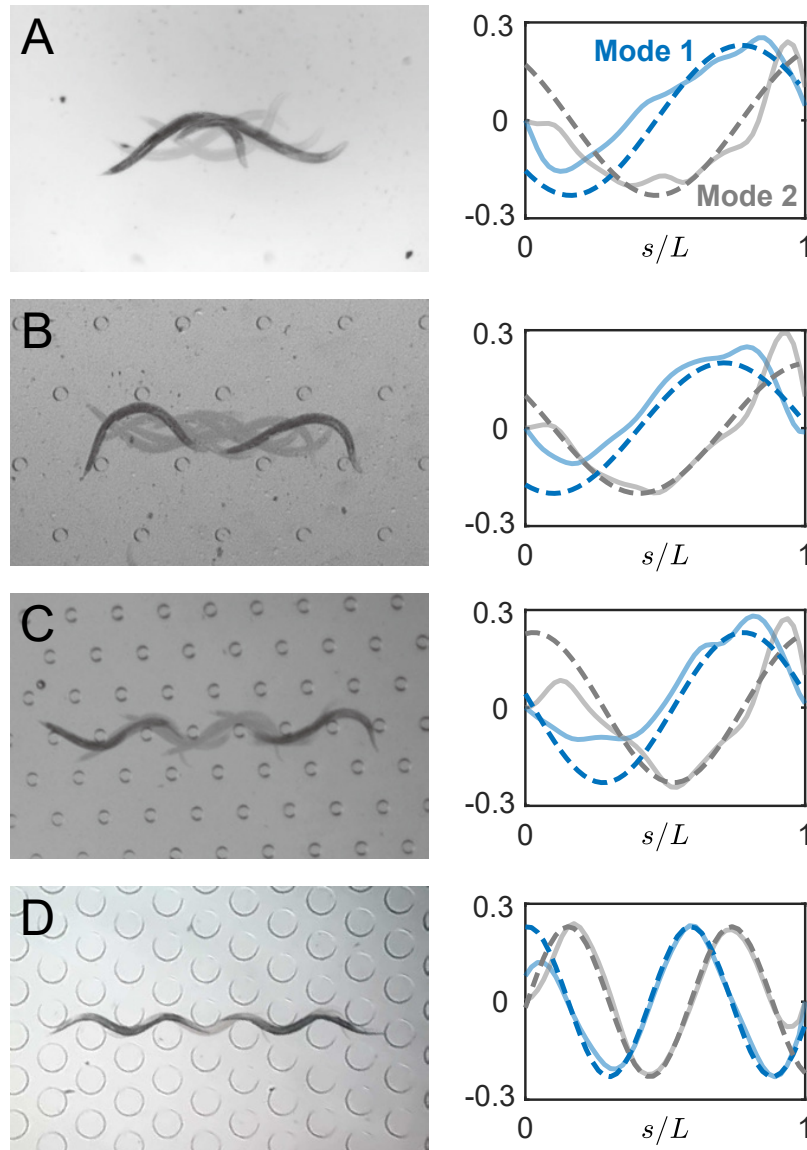


Fig. S2: Overlaid photos of *C. elegans* movements and their low dimensional representations in (A) open fluid, (B) a sparse lattice, (C) a medium lattice, and (D) a dense lattice. Solid lines are the first two dominant relative curvature (κL) PCA modes and dashed lines are the best fits to sin and cos functions (see text).

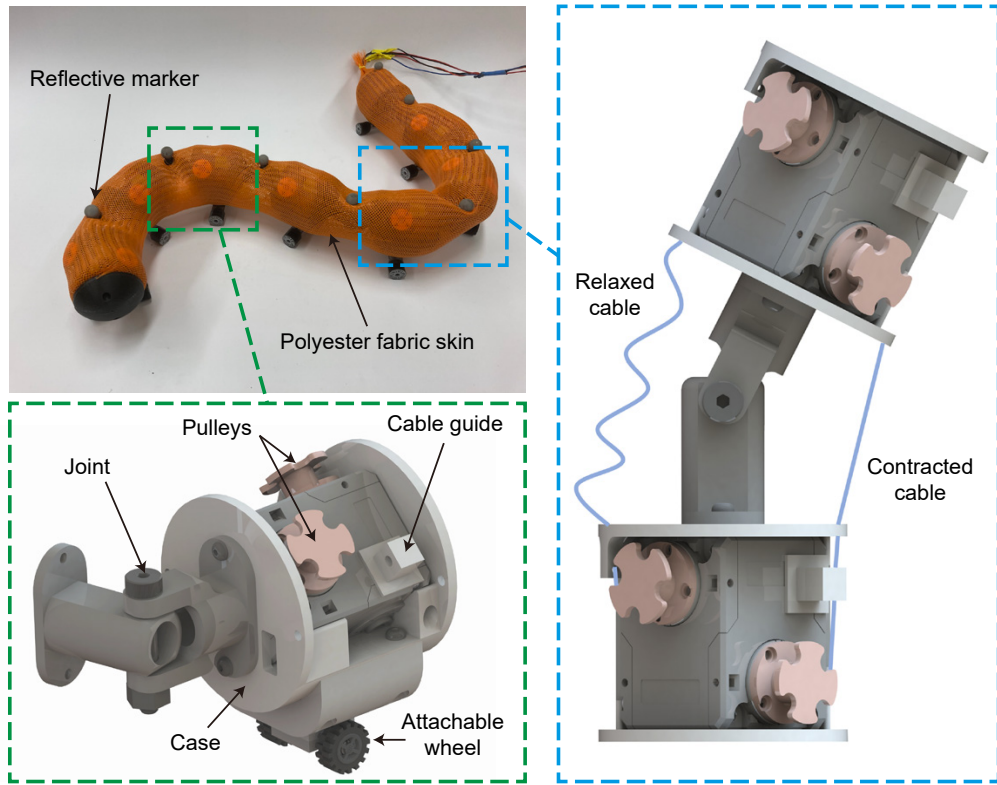


Fig. S3: A photo and computer aided design drawings detailing components of the robophysical model.

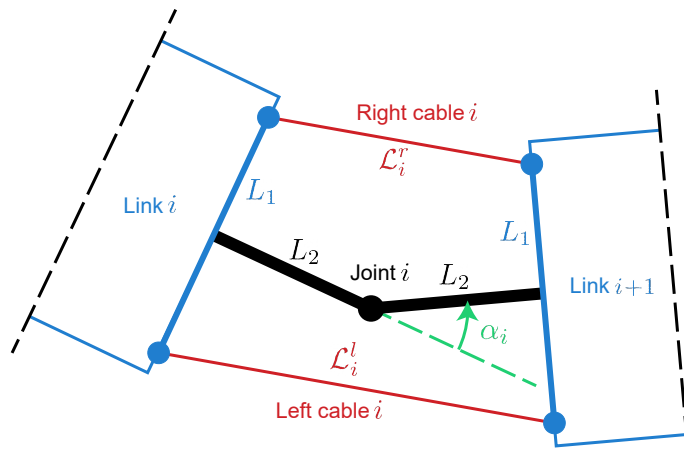
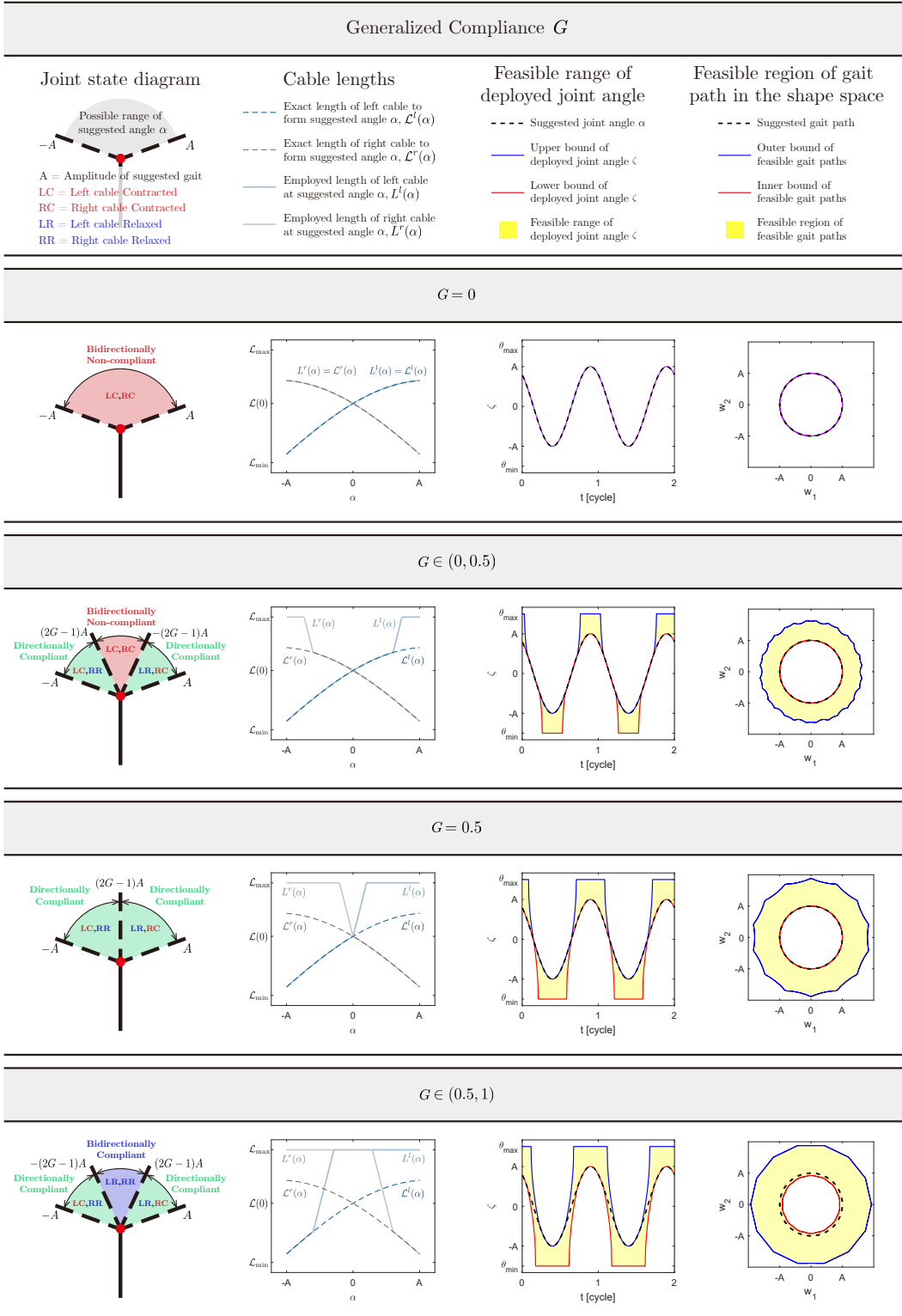


Fig. S4: Geometry of the joint mechanical design for the calculation of exact lengths of cables \mathcal{L}_i^l and \mathcal{L}_i^r to strictly form a suggested angle α_i .

Generalized Compliance G



(Con'd)

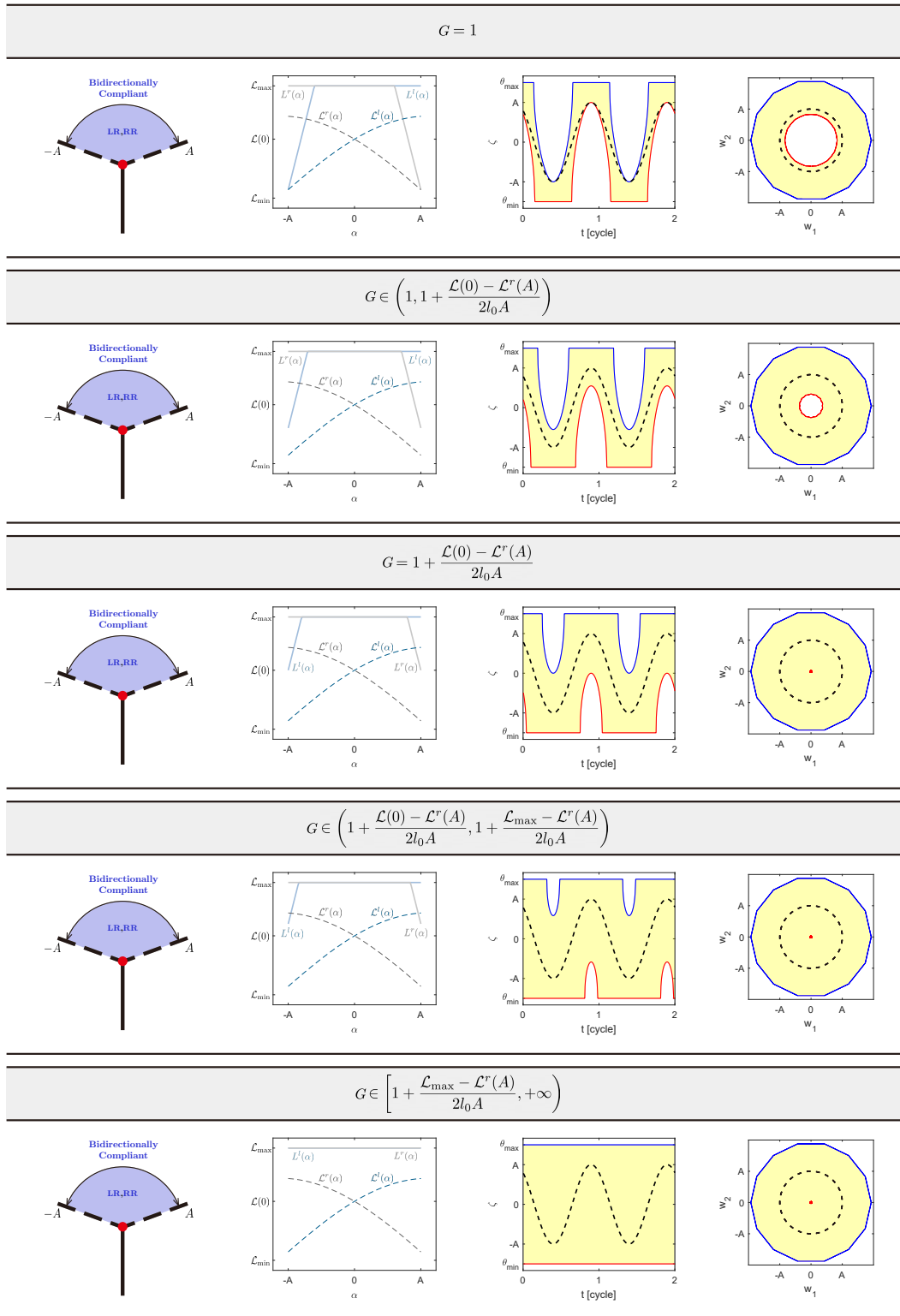


Fig. S5: An overview of behaviors that one single joint and the whole robophysical model can display with varied generalized compliance value G . The first schematic in each row shows the state of the joint, left and right cables depending on which region the suggested joint angle falls into. The second plot in each row illustrates the actual lengths according to the control scheme comparing with the exact lengths of left and right cables on either sides of the joint as a function of the suggested joint angle. The third plot in each row illustrates the feasible range of all possible emergent joint angle, showing how much a single joint angle could deviate from the suggested joint angle by perturbation of external forces. The last figure in each row depicts the feasible region of all possible emergent gait paths of the robophysical model in the shape space.

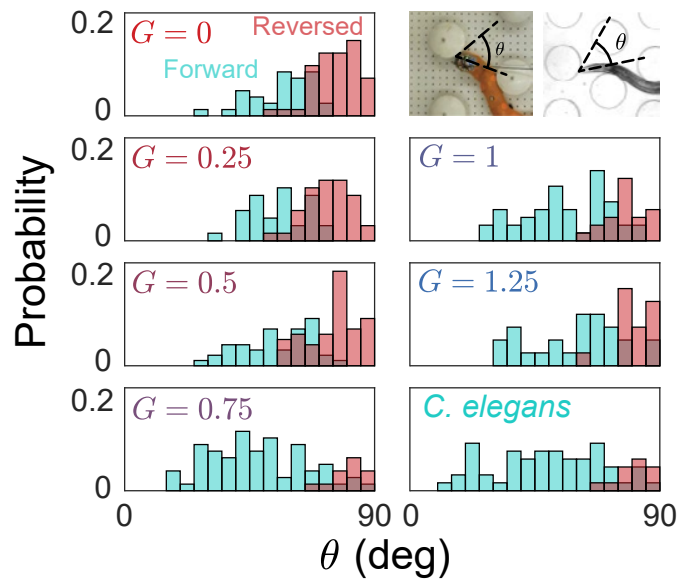


Fig. S6: Head collision angle probability distributions categorized by post-collision motion directions (forward or reversed) in the robo-physical model with varied G , comparing to *C. elegans* (for each plot, sample size > 100), where the robo-physical model with $G = 0.75$ closely captures *C. elegans* behaviors.

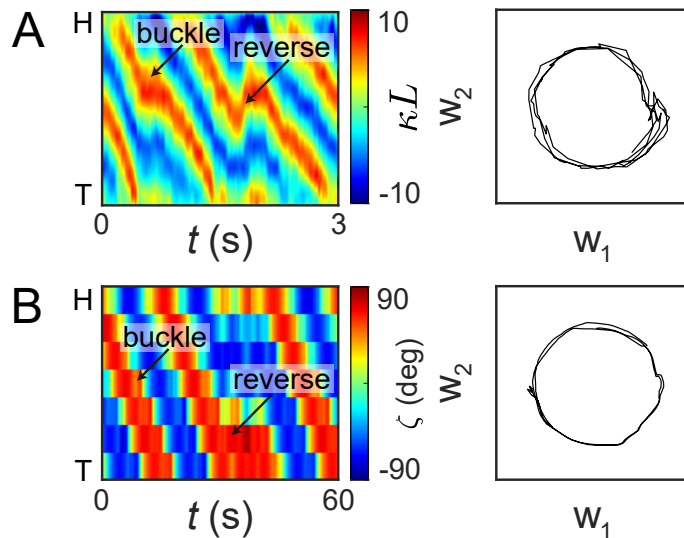


Fig. S7: Similar body kinematics displayed by (A) *C. elegans* and (B) the closed-loop robo-physical model with $G = 0.75$ in dense lattices, by comparing body curvature (emergent joint angles) heatmaps and gait trajectories in the shape space.

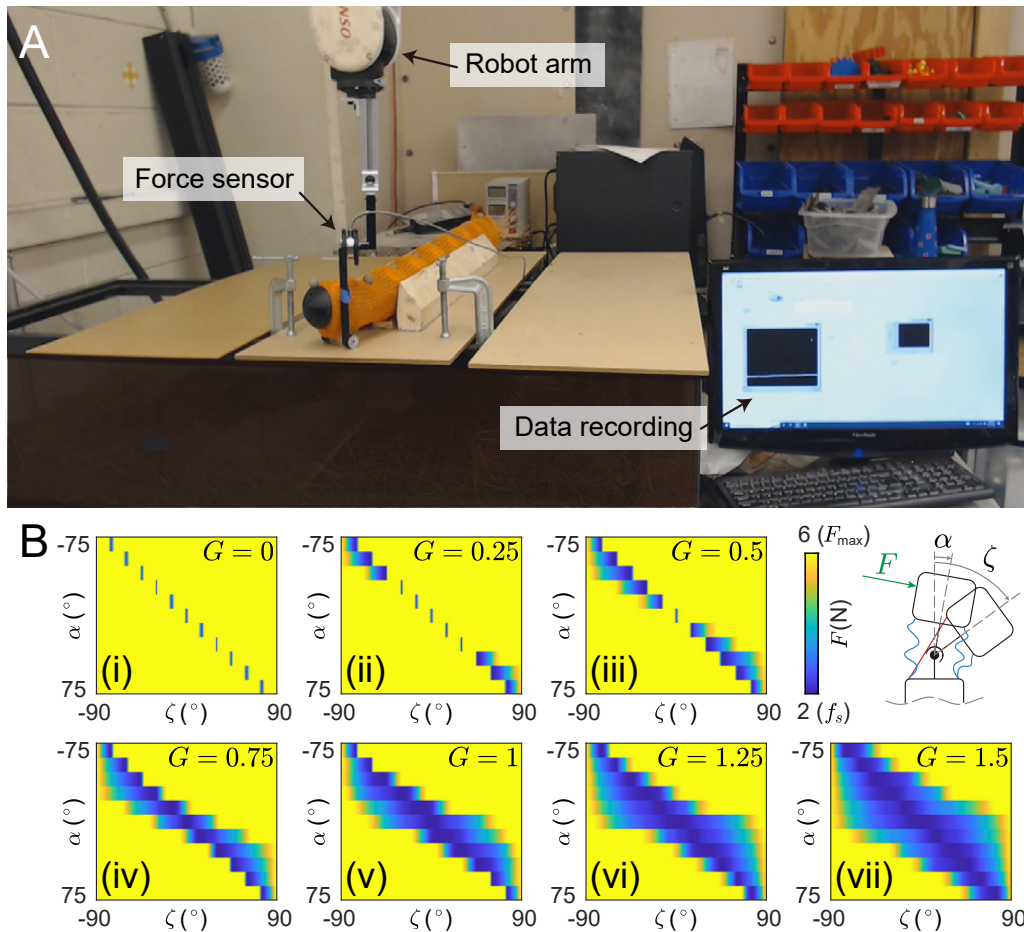


Fig. S8: Force-deformation property characterization for the robophysical model. (A) The experiment setup. (B) Force-deformation heatmaps for the robophysical model with varied G , indicating the robophysical model as a programmable functional smart material.

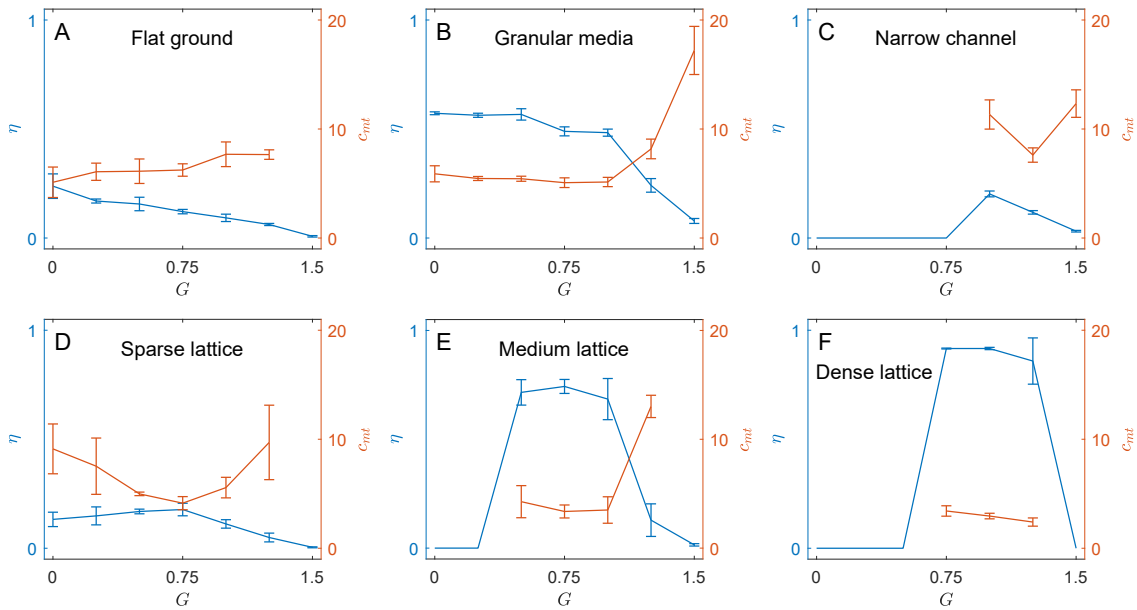


Fig. S9: Robot locomotion speed (wave efficiency, η) and mechanical cost of transport (c_{mt}) in different environments: (A) flat ground, (B) granular material (5 mm plastic spheres), (C) a narrow channel (18 cm width), (D) a sparse lattice, (E) a medium lattice, and (F) a dense lattice.

References

1. J. Gau, *et al.*, *Proceedings of the Royal Society B* **288**, 20210352 (2021).
2. R. M. Alexander, *Principles of animal locomotion* (Princeton University Press, 2003).
3. P. E. Schiebel, *et al.*, *Proceedings of the National Academy of Sciences* **116**, 4798 (2019).
4. C. Fang-Yen, *et al.*, *Proceedings of the National Academy of Sciences* **107**, 20323 (2010).
5. J. G. White, E. Southgate, J. N. Thomson, S. Brenner, *et al.*, *Philos Trans R Soc Lond B Biol Sci* **314**, 1 (1986).
6. A.-S. Chiang, *et al.*, *Current biology* **21**, 1 (2011).
7. E. A. Naumann, *et al.*, *Cell* **167**, 947 (2016).

8. S. W. Oh, *et al.*, *Nature* **508**, 207 (2014).
9. S. Sponberg, R. Full, *Journal of Experimental Biology* **211**, 433 (2008).
10. D. A. Winter, *Biomechanics and motor control of human movement* (John Wiley & Sons, 2009).
11. L. Ristroph, *et al.*, *Proceedings of the National Academy of Sciences* **107**, 4820 (2010).
12. M. A. Daley, J. R. Usherwood, G. Felix, A. A. Biewener, *Journal of experimental biology* **209**, 171 (2006).
13. M. Sitti, *Extreme Mechanics Letters* **46**, 101340 (2021).
14. R. Pfeifer, M. Lungarella, F. Iida, *science* **318**, 1088 (2007).
15. R. Pfeifer, J. Bongard, *How the body shapes the way we think: a new view of intelligence* (MIT press, 2006).
16. F. Iida, F. Giardina, *Annual Review of Control, Robotics, and Autonomous Systems* **6** (2022).
17. R. Gaymer, *Nature* **234**, 150 (1971).
18. B. C. Jayne, *Copeia* pp. 915–927 (1986).
19. M.-A. Félix, C. Braendle, *Current biology* **20**, R965 (2010).
20. N. Cohen, J. H. Boyle, *Contemporary Physics* **51**, 103 (2010).
21. N. Gravish, G. V. Lauder, *Journal of Experimental Biology* **221**, jeb138438 (2018).
22. A. J. Ijspeert, *science* **346**, 196 (2014).
23. J. Aguilar, *et al.*, *Reports on Progress in Physics* **79**, 110001 (2016).

24. R. Full, D. Koditschek, *Journal of experimental biology* **202**, 3325 (1999).
25. F. Meyer, A. Spröwitz, L. Berthouze, *Advanced Robotics* **20**, 953 (2006).
26. S. Collins, A. Ruina, R. Tedrake, M. Wisse, *Science* **307**, 1082 (2005).
27. G. Bleedt, *et al.*, *2018 IEEE/RSJ International Conference on Intelligent Robots and Systems (IROS)* (IEEE, 2018), pp. 2245–2252.
28. R. Altendorfer, *et al.*, *Autonomous Robots* **11**, 207 (2001).
29. M. H. Dickinson, F.-O. Lehmann, S. P. Sane, *Science* **284**, 1954 (1999).
30. S. Hirose, M. Mori, *2004 IEEE International Conference on Robotics and Biomimetics* (IEEE, 2004), pp. 1–7.
31. P. Liljebäck, K. Y. Pettersen, Ø. Stavdahl, J. T. Gravdahl, *Robotics and Autonomous systems* **60**, 29 (2012).
32. A. Crespi, A. J. Ijspeert, *IEEE Transactions on robotics* **24**, 75 (2008).
33. C. Wright, *et al.*, *2007 IEEE/RSJ International Conference on Intelligent Robots and Systems* (IEEE, 2007), pp. 2609–2614.
34. J. Liu, Y. Tong, J. Liu, *Robotics and Autonomous Systems* **141**, 103785 (2021).
35. T. Wang, J. Whitman, M. Travers, H. Choset, *2020 American Control Conference (ACC)* (IEEE, 2020), pp. 2458–2463.
36. F. Sanfilippo, *et al.*, *Applied Sciences* **7**, 336 (2017).
37. T. Kano, T. Sato, R. Kobayashi, A. Ishiguro, *Bioinspiration & biomimetics* **7**, 046008 (2012).

38. M. Luo, M. Agheli, C. D. Onal, *Soft Robotics* **1**, 136 (2014).
39. C. Branyan, *et al.*, *2017 IEEE International Conference on Robotics and Biomimetics (RO-BIO)* (IEEE, 2017), pp. 282–289.
40. X. Qi, T. Gao, X. Tan, *Soft Robotics* (2022).
41. P. E. Schiebel, M. C. Maisonneuve, K. Diaz, J. M. Rieser, D. I. Goldman, *Biomimetic and Biohybrid Systems: 9th International Conference, Living Machines 2020, Freiburg, Germany, July 28–30, 2020, Proceedings 9* (Springer, 2020), pp. 300–311.
42. J. H. Boyle, S. Johnson, A. A. Dehghani-Saniij, *IEEE/ASME Transactions on Mechatronics* **18**, 439 (2012).
43. P. Racioppo, P. Ben-Tzvi, *IEEE/ASME Transactions On Mechatronics* **24**, 893 (2019).
44. L. R. Varshney, B. L. Chen, E. Paniagua, D. H. Hall, D. B. Chklovskii, *PLoS computational biology* **7**, e1001066 (2011).
45. C. Fang-Yen, M. J. Alkema, A. D. Samuel, *Philosophical Transactions of the Royal Society B: Biological Sciences* **370**, 20140212 (2015).
46. J. P. Nguyen, *et al.*, *Proceedings of the National Academy of Sciences* **113**, E1074 (2016).
47. J. M. Rieser, *et al.*, *arXiv preprint arXiv:1906.11374* (2019).
48. B. Chong, T. Wang, E. Erickson, P. J. Bergmann, D. I. Goldman, *Proceedings of the National Academy of Sciences* **119**, e2118456119 (2022).
49. G. J. Stephens, B. Johnson-Kerner, W. Bialek, W. S. Ryu, *PLoS computational biology* **4**, e1000028 (2008).

50. S. Park, *et al.*, *PloS one* **3**, e2550 (2008).
51. S. Hirose, *Snake-Like Locomotors and Manipulators* (1993).
52. H. Cui, *et al.*, *Science* **376**, 1287 (2022).
53. C. Kaspar, B. Ravoo, W. G. van der Wiel, S. Wegner, W. Pernice, *Nature* **594**, 345 (2021).
54. B. Zhao, P. Khare, L. Feldman, J. A. Dent, *Journal of Neuroscience* **23**, 5319 (2003).
55. D. B. Doroquez, C. Berciu, J. R. Anderson, P. Sengupta, D. Nicastro, *Elife* **3**, e01948 (2014).
56. H. Hauser, A. J. Ijspeert, R. M. Fuchslin, R. Pfeifer, W. Maass, *Biological cybernetics* **105**, 355 (2011).
57. C. Laschi, B. Mazzolai, *IEEE Robotics & Automation Magazine* **23**, 107 (2016).
58. J. H. Long Jr, *American zoologist* **38**, 771 (1998).
59. M. Backholm, W. S. Ryu, K. Dalnoki-Veress, *Proceedings of the National Academy of Sciences* **110**, 4528 (2013).
60. T. Kano, A. Ishiguro, *2013 IEEE/RSJ International Conference on Intelligent Robots and Systems* (IEEE, 2013), pp. 3273–3278.
61. M. J. Travers, J. Whitman, P. E. Schiebel, D. I. Goldman, H. Choset, *Robotics: Science and Systems* (2016), vol. 12.
62. G. Sartoretti, T. Wang, G. Chuang, Q. Li, H. Choset, *2021 IEEE International Conference on Robotics and Automation (ICRA)* (IEEE, 2021), pp. 9276–9282.
63. Z. Bing, *et al.*, *Frontiers in Neurorobotics* **14**, 591128 (2020).

64. K. G. Hanssen, A. A. Transeth, F. Sanfilippo, P. Liljebäck, Ø. Stavdahl, *2020 IEEE 16th International Workshop on Advanced Motion Control (AMC)* (IEEE, 2020), pp. 98–104.
65. J. Yuan, D. M. Raizen, H. H. Bau, *Proceedings of the National Academy of Sciences* **111**, 6865 (2014).
66. R. D. Maladen, Y. Ding, P. B. Umbanhowar, D. I. Goldman, *The International Journal of Robotics Research* **30**, 793 (2011).
67. B. Chong, *et al.*, *arXiv preprint arXiv:2302.06561* (2023).
68. T. Wang, *et al.*, *2022 International Conference on Robotics and Automation (ICRA)* (IEEE, 2022), pp. 01–07.
69. B. Chong, *et al.*, *The International Journal of Robotics Research* **40**, 1547 (2021).
70. T. Takemori, M. Tanaka, F. Matsuno, *IEEE Transactions on Robotics* (2022).
71. A. J. Ijspeert, *Neural networks* **21**, 642 (2008).
72. R. Thandiackal, *et al.*, *Science Robotics* **6**, eabf6354 (2021).
73. G. Bellegarda, A. Ijspeert, *IEEE Robotics and Automation Letters* **7**, 12547 (2022).
74. T. Haarnoja, H. Tang, P. Abbeel, S. Levine, *International conference on machine learning* (PMLR, 2017), pp. 1352–1361.
75. S. Ramasamy, R. L. Hatton, *Physical Review E* **103**, 032605 (2021).
76. G. Strang, *Introduction to linear algebra*, vol. 3 (Wellesley-Cambridge Press Wellesley, MA, 1993).
77. J. M. Rieser, *et al.*, *Physical Review E* **99**, 022606 (2019).

78. J. Gray, G. Hancock, *Journal of Experimental Biology* **32**, 802 (1955).
79. J. Sznitman, X. Shen, R. Sznitman, P. E. Arratia, *Physics of Fluids* **22**, 121901 (2010).
80. S. Alben, *Physical Review E* **99**, 062402 (2019).
81. G. Gabrielli, *Mech. Eng.(ASME)* **72**, 775 (1950).
82. S. Seok, *et al.*, *2013 IEEE International Conference on Robotics and Automation* (IEEE, 2013), pp. 3307–3312.
83. U. Saranli, M. Buehler, D. E. Koditschek, *The International Journal of Robotics Research* **20**, 616 (2001).
84. R. L. Hatton, Y. Ding, H. Choset, D. I. Goldman, *Physical review letters* **110**, 078101 (2013).
85. A. Parashar, R. Lycke, J. A. Carr, S. Pandey, *Biomicrofluidics* **5**, 024112 (2011).